JGR Atmospheres

RESEARCH ARTICLE
10.1029/2021JD034865

Special Section:
Atmospheric Rivers: Intersection of Weather and Climate

Multi-GNSS Airborne Radio Occultation Observations as a Complement to Dropsondes in Atmospheric River Reconnaissance

J. S. Haase[1], M. J. Murphy[1], B. Cao[1], F. M. Ralph[2], M. Zheng[2], and L. Delle Monache[2]

[1]Scripps Institution of Oceanography, University of California San Diego, La Jolla, CA, USA, [2]Center for Western Weather and Water Extremes, Scripps Institution of Oceanography, University of California San Diego, La Jolla, CA, USA

Key Points:

- Flights over northeast Pacific atmospheric rivers provide dense airborne radio occultation and dropsonde data for assimilation in models
- The first Galileo RO profiles are compared with nearby Global Positioning System (GPS) profiles to assess accuracy in the troposphere
- The model refractivity anomaly distinguishes key characteristics of the atmospheric river including the low-level jet and tropopause fold

Supporting Information:

Supporting Information may be found in the online version of this article.

Correspondence to:

J. S. Haase,
jhaase@ucsd.edu

Citation:

Haase, J. S., Murphy, M. J., Cao, B., Ralph, F. M., Zheng, M., & Delle Monache, L. (2021). Multi-GNSS airborne radio occultation observations as a complement to dropsondes in atmospheric river reconnaissance. *Journal of Geophysical Research: Atmospheres*, *126*, e2021JD034865. https://doi.org/10.1029/2021JD034865

Received 5 MAR 2021
Accepted 16 OCT 2021

Author Contributions:

Conceptualization: J. S. Haase
Data curation: J. S. Haase
Formal analysis: M. J. Murphy, B. Cao
Funding acquisition: J. S. Haase
Investigation: J. S. Haase, M. J. Murphy, M. Zheng
Methodology: J. S. Haase, M. J. Murphy, B. Cao
Project Administration: J. S. Haase
Resources: F. M. Ralph
Software: J. S. Haase
Supervision: J. S. Haase

Abstract Variations in the water vapor that atmospheric rivers (ARs) carry toward North America within Pacific storms strongly modulates the spatiotemporal distribution of west-coast precipitation. The "AR Recon" program was established to improve forecasts of landfalling Pacific-coast ARs and their associated precipitation. Dropsondes are deployed from weather reconnaissance aircraft and pressure sensors have been added to drifting ocean buoys to fill a major gap in standard weather observations, while research is being conducted on the potential for airborne Global Navigation Satellite System (GNSS) radio occultation (ARO) to also contribute to forecast improvement. ARO further expands the spatial coverage of the data collected during AR Recon flights. This study provides the first description of these data, which provide water vapor and temperature information typically as far as 300 km to the side of the aircraft. The first refractivity profiles from European Galileo satellites are provided and their accuracy is evaluated using the dropsondes. It is shown that spatial variations in the refractivity anomaly (difference from the climatological background) are modulated by AR features, including the low-level jet and tropopause fold, illustrating the potential for RO measurements to represent key AR characteristics. It is demonstrated that assimilation of ARO refractivity profiles can influence the moisture used as initial conditions in a high-resolution model. While the dropsonde measurements provide precise, in situ wind, temperature and water vapor vertical profiles beneath the aircraft, and the buoys provide surface pressure, ARO provides complementary thermodynamic information aloft in broad areas not otherwise sampled at no additional expendable cost.

Plain Language Summary Aircraft are deployed to make extraobservations and improve forecasts of the atmospheric rivers that carry moisture toward the coast of North America in northeast Pacific storms. Dropsondes are released from the aircraft to measure moisture, temperature and winds as they descend. We have increased the coverage of the aircraft measurements by making simultaneous measurements of the atmosphere using Global Positioning System (GPS) signals, and for the first time, signals from the European Galileo satellite system which provides 50% more radio occultation measurements. These airborne radio occultation (ARO) measurements of the refractive index of the atmosphere are based on travel time delays of the satellite signals, and are used to provide refractivity, moisture, and temperature profile information to the sides of the aircraft. The observations are assimilated into a mesoscale weather model to improve the initial moisture conditions used for the weather forecast. Cross sections through the updated model volume show variations in the refractivity that correspond to the atmospheric river features at low levels and cold front features at upper levels.

1. Introduction

Atmospheric rivers (ARs) are long narrow filaments of strong water vapor transport within the precold-frontal region of an extratropical cyclone (e.g., Figure 1), and they account for 90% of the meridional water vapor transport in midlatitudes (Neiman, Ralph, Wick, Lundquist, & Dettinger, 2008; Ralph et al., 2004; Zhu & Newell, 1998). ARs can produce intense extended periods of orographic precipitation when they are uplifted over coastal mountain ranges, due to high integrated water vapor transport (IVT) within the prefrontal low-level jet. Landfalling ARs contribute roughly 25%–50% of the precipitation falling in winter storms on

Validation: M. J. Murphy, B. Cao
Visualization: J. S. Haase, M. J. Murphy, B. Cao
Writing – original draft: J. S. Haase
Writing – review & editing: M. J. Murphy, F. M. Ralph, M. Zheng, L. Delle Monache

the west-coast of North America (Dettinger et al., 2011; Ralph et al., 2013; Rutz et al., 2014). They are also the major flood-makers for the Western US, where they account for 84% of all flood damages on average (Corringham et al., 2019). Their combined roles in providing beneficial water supply and in flooding has led to the creation of a scale to provide situational awareness (Ralph et al., 2019). The orientation and location of the highest moisture flux within the low-level jet at landfall greatly impacts the predicted precipitation, runoff, and potential flooding in local watersheds (e.g., Martin et al., 2019; Ralph et al., 2013).

The Atmospheric Rivers Reconnaissance Program (AR Recon) led by the Center for Western Weather and Water Extremes (CW3E) and the National Weather Service National Centers for Environmental Prediction (NCEP) was designed to collect and assimilate supplementary weather observations into numerical weather prediction (NWP) models to improve forecast precipitation over the Pacific-coast of the United States (PACUS; Ralph et al., 2019, 2020). The series of AR Recon field campaigns in 2016, 2018, 2019, and 2020 (www.cw3e.ucsd.edu/ARRecon/) have been supported by stakeholders such as the Army Corps of Engineers and the California Department of Water Resources, because of their importance to flood management and reservoir operations linked to water resources management (Ralph et al., 2020). AR Recon is particularly focused on collecting dropsonde data from weather reconnaissance aircraft to improve NWP by reducing errors in the initial conditions used by models in and around nascent and mature ARs offshore (e.g., Figure 1; Ralph et al., 2020; Zheng et al., 2021). AR Recon also collaborates with the Global Drifter Program (Centurioni, 2018; Horanyi et al., 2017) to add pressure sensors to drifting buoys and helps deploy them in areas where ARs or their precursors are common. Observations are assimilated into the NCEP, European Center for Medium-range Weather Forecasting (ECMWF), US Navy, and other global models. Zheng et al. (2021) documented the relative sparsity and degraded quality of observations in the vicinity of oceanic ARs due to the presence of thick clouds and precipitation, and to limited availability of surface-based observations that are much more common over land, leading to the potential for large model errors. Forecast busts have been associated with inaccurate descriptions of mesoscale frontal waves and other features that modify the intensity and location of the moist prefrontal low-level jet that is responsible for the intense orographic precipitation at landfall (Martin et al., 2019).

The dropsonde observations are targeted at physical and dynamical features that control the storm evolution. Physical structures, including the ARs themselves, potential vorticity streamers, shortwave troughs, and other important meteorological conditions are identified as possible targets based on their roles in modulating initial condition errors. In addition, numerical modeling tools have been developed to quantitatively identify areas where high sensitivity of the forecast precipitation to model errors is present. AR Recon includes techniques for targeted observing guidance such as adjoint methods (Doyle et al., 2014; Reynolds et al., 2019) and ensemble-based methods (Ancell & Hakim, 2007; Majumdar et al., 2010; Torn & Hakim, 2008) for assessing the sensitivity of forecasts to model errors and uncertainties at earlier times. These areas can correlate well with physical structures, for example as shown by Reynolds et al. (2019), where a composite of 60 cases found that the moist-adjoint-based targets corresponded closely to the position of the AR offshore. Targeted dropsondes sample these regions directly beneath the flight path, but because of the geographically extended nature of the physical structures or adjoint/ensemble sensitivity areas being targeted (Majumdar, 2016), it is highly advantageous to also sample the region surrounding the flight path.

The objective of this study is to examine the potential for Global Navigation Satellite System (GNSS) airborne radio occultation (ARO) to contribute to AR Recon by providing many additional observations in the extended region surrounding the flight path to better cover the physical targets or adjoint/ensemble-based sensitive regions. Dropsonde observations are optimal because they precisely measure thermodynamic variables directly and include wind, with high spatial resolution in regions of strong IVT gradients, for example, in transects across the short dimension of the AR. However, ARO has several advantages in that profiles can be collected during the entire duration of reconnaissance flights at no additional expendable cost, adjacent to and over airspace that may be restricted for dropsonde sampling, and can similarly sample regions of heavy rain and clouds. ARO extends the observed area, often serendipitously sampling the longer dimension of the AR during the ferry flights.

ARO is a technique that measures the refractive delay in the propagation of GNSS signals arriving nearly horizontally at the aircraft from rising and setting GNSS satellites (Haase et al., 2014). The refractive delay

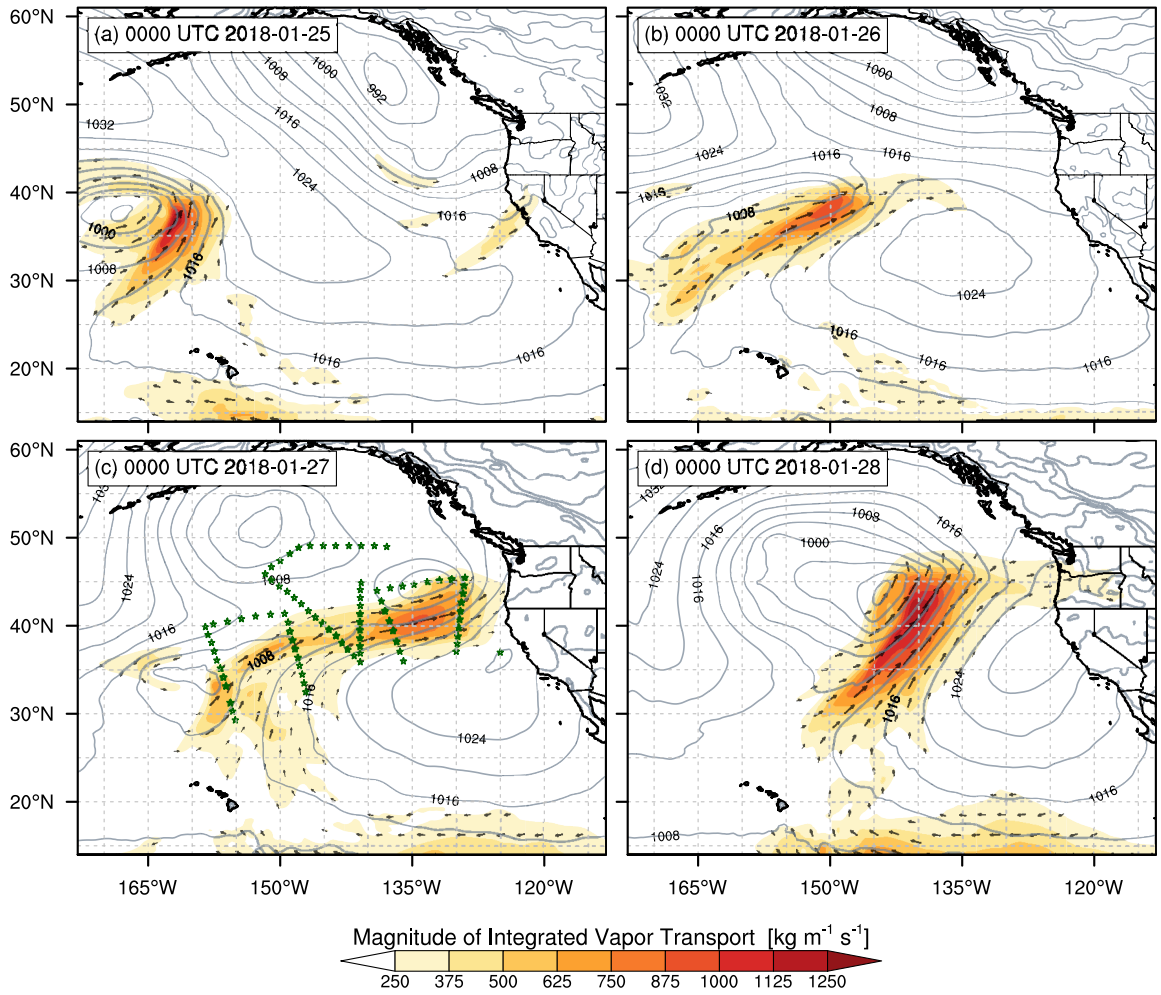

Figure 1. Mean sea level pressure [contours, hPa] and integrated water vapor transport (IVT) (shaded, kg m^{-1} s^{-1}) derived from the ECMWF Reanalysis 5 (ERA5) product are shown for (a) 00 UTC January 25; (b) 00 UTC January 26; (c) 00 UTC January 27; (d) 00 UTC January 28, 2018. Green stars indicate the locations of the dropsondes released on January 27.

is used to derive profiles of atmospheric refractivity, pressure, temperature, and water vapor. The integrated measurements sample the atmosphere to the side of the aircraft resulting in a profile representative of the environment surrounding the AR (Figure 2c). The ARO technique is similar to radio occultation from Low Earth Orbiting (LEO) satellites (Kursinski et al., 1997) implemented in the Constellation Observing System for Meteorology Ionosphere and Climate (COSMIC)/Formosa Satellite-3 (FORMOSAT-3) constellation (Anthes et al., 2008; Ho, Anthes, et al., 2020) and the new COSMIC-2 tropical constellation (Schreiner et al., 2020).

ARO measurements have been made simultaneously with dropsondes in targeted tropical cyclone flights (Haase et al., 2014; Murphy et al., 2015; Wang et al., 2017) and their impact was assessed in a case study for hurricane Karl (Chen et al., 2018). The retrieval method introduces uncertainties because of the ambiguity between temperature and water vapor, and also because of horizontal variations in atmospheric structure, so the study of hurricane Karl used an excess phase observation operator that allows variations in the horizontal to be accommodated in the data assimilation (Chen et al., 2009, 2018; Ma et al., 2009); however this is computationally expensive. Operationally, LEO RO refractivity and bending angle data are assimilated on a routine basis, and have improved global NWP models because of their high accuracy and vertical resolution near the tropopause (Aparicio & Deblonde, 2008; Bauer et al., 2014; Cucurull et al., 2007; Healy & Thepaut, 2006; Poli et al., 2009; Rennie, 2010). Nevertheless, challenges with assimilating LEO RO in the lower troposphere arise from relatively sparse coverage, particularly for ARs (i.e., Ma et al., 2011) and

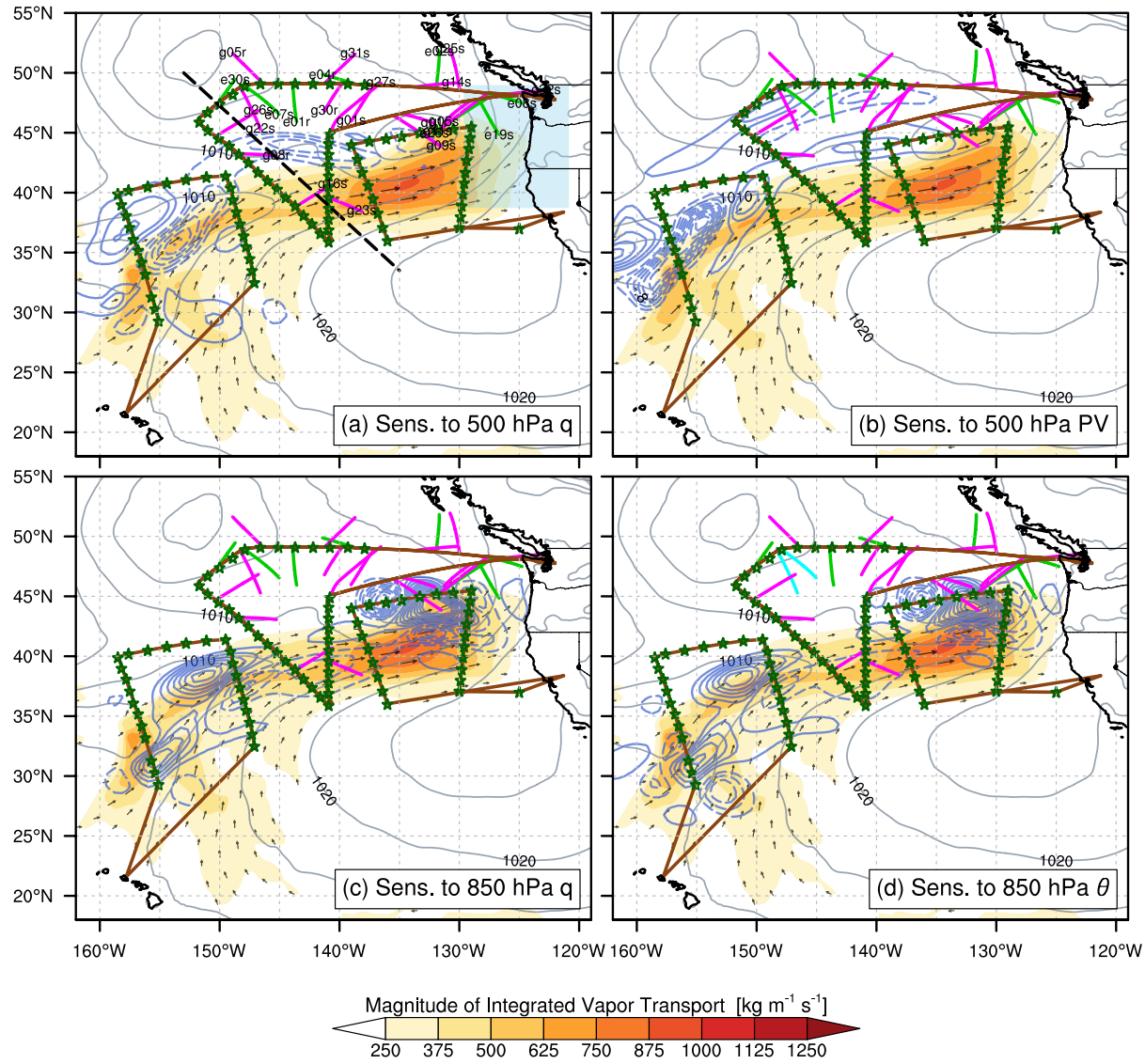

Figure 2. Flight tracks (solid brown) of the G-IV and two C-130 aircraft during the first Intensive Observing Period of AR Recon 2018 (IOP1). Shading and vectors show integrated vapor transport (kg m^{-1} s^{-1}) and gray contours are sea level pressure from the ERA5 product valid at 00 UTC on January 27, 2018. Green stars indicate the locations where dropsondes were released. Airborne radio occultation (ARO) profiles retrieved from Global Positioning System (GPS) and Galileo satellites are denoted by magenta and green lines, respectively. For each occultation, the horizontal locations of the tangent points are shown, starting from the highest tangent point adjacent to the flight path and ending at the lowest tangent point furthest from the flight path. (a) Occultations are labeled with GPS and Galileo satellite number (PRN) (prefixed with g for GPS, e for Galileo, and suffixed with r for rising and s for setting). Dashed line indicates the location of the cross section in Figure 8. Purple contours are sensitivity to specific humidity at 500 hPa. (b) Same as (a) but purple contours are sensitivity to potential vorticity at 500 hPa. (c) Purple contours are sensitivity to specific humidity at 850 hPa. (d) Purple contours are sensitivity to potential temperature at 850 hPa. The occultations of e07s and g22s (highlighted in cyan in (d), are compared in Figure 5.

typically down-weighted quality in the lower troposphere compared with the upper troposphere and lower stratosphere (Chen et al., 2009; Healy, 2013). For this study, we use refractivity as the parameter of choice in the comparisons with other data sets to avoid the ambiguity in the retrieval of temperature and humidity from refractivity. We also use refractivity in the simplified data assimilation tests included in this work.

The study presented here using ARO builds on earlier studies using COSMIC RO data to study ARs. Neiman, Ralph, Wick, Kuo, et al. (2008) showed that RO data could elucidate the structure of an AR over the northeast Pacific, including changes of >1 g/kg to the lower tropospheric water vapor mixing ratio, which was more than a 10% change from the background. In addition, the data assimilation study by Ma et al. (2011) showed that assimilation of the COSMIC RO data over a broad area of the eastern Pacific was

able to move the position of the predicted AR several hours later, indicating the potential for RO assimilation to be impactful in AR landfall prediction. The objective of the deployment for this study is to augment the number of profiles in the nearby environment of the AR by using RO on the reconnaissance aircraft platform.

As a first step toward including ARO data along with dropsondes into the National Winter Season Operations Plan (OFCM, 2019), we describe the accuracy of the ARO observations, and carry out a data assimilation demonstration. In Section 2, we give an overview of the ARO method. Section 3 describes the ARO and dropsonde observations collected during a reconnaissance flight and case study of an AR on January 26 and 27, 2018. In Section 4, we demonstrate the instrumental accuracy of the ARO technique using the first Galileo profiles ever recorded, and show the consistency of the ARO data with the dropsonde data. We also compare the data sets with model fields from the ECMWF Reanalysis 5 (ERA5) product, and mesoscale model runs based on the CW3E high-resolution version of the Weather Research and Forecasting (WRF; Skamarock et al., 2008) modeling system optimized for AR prediction (Martin et al., 2018). In Section 5, we describe the results of mesoscale modeling data assimilation experiments to test the hypothesis that ARO observations add new and accurate information to the model initial conditions, to impact the water vapor in areas that are not sampled by the dropsondes. Section 6 explains the unique characteristics of ARs that are particularly well-delineated by refractivity and motivate enhanced use of RO, and a dedicated research effort to increase the quality of the retrieved data in the lower troposphere. It provides a discussion on the perspectives for the use of ARO observations in an operational setting, and the need for comprehensive data assimilation experiments to address quantitatively the impact on precipitation forecasts. The conclusions are presented in Section 7 to support incorporating ARO into operational AR Recon.

2. The Airborne Radio Occultation Method

The RO technique, in general, is known for providing high vertical resolution all-weather observations in heavy clouds and precipitation. ARO concentrates these observations within the environment of a targeted storm system. Similar to LEO RO, nearly horizontally propagating radio waves arriving at the antenna from angles below the local horizon undergo significant refractive bending and a Doppler shift due to variations of the atmospheric refractive index at each level of the atmosphere through which the raypath passes. An atmospheric profile is derived from precise measurements of the time delay, Doppler shift, and refractive bending angle of the radio wave raypath using an Abel transform and assuming spherically symmetric atmospheric layers. The refractivity or refractive index in the neutral atmosphere depends on the pressure (hPa), P, temperature (K), T, and water vapor partial pressure (hPa), e:

$$N = \left(n-1\right)\times 10^{6} = \frac{77.6890\,P}{T} - \frac{6.3938\,e}{T} + \frac{3.75463\times 10^{5}\,e}{T^{2}} \quad (1)$$

(Rüeger, 2002). Refractivity varies primarily in the vertical direction and increases exponentially toward the surface in a manner similar to density. In the standard retrieval process for both LEO RO and ARO, the integrated delay over a nearly horizontal raypath is reduced to a representative value of refractivity at the tangent point (point of closest approach of the raypath to the Earth) where the propagation delay is concentrated. The ARO retrieval technique is adapted to the slowly moving airborne geometry where the tangent point drifts horizontally during the occultation (Figure 3) and corrects for the refractive delay accumulated above the aircraft flight level.

Simulation studies have shown the sensitivity of the ARO technique to temperature and water vapor variations in the atmosphere below flight level (Healy et al., 2002; Lesne et al., 2002; Xie et al., 2008). Observations over land and ocean (Chen et al., 2018; Wang et al., 2017; Xie et al., 2018) have been used to demonstrate the successful application of the technique from ~2 km to flight level when using the GNSS Instrument System for Multistatic and Occultation Sensing (GISMOS) system open-loop tracking GPS signal recorder (Garrison et al., 2007).

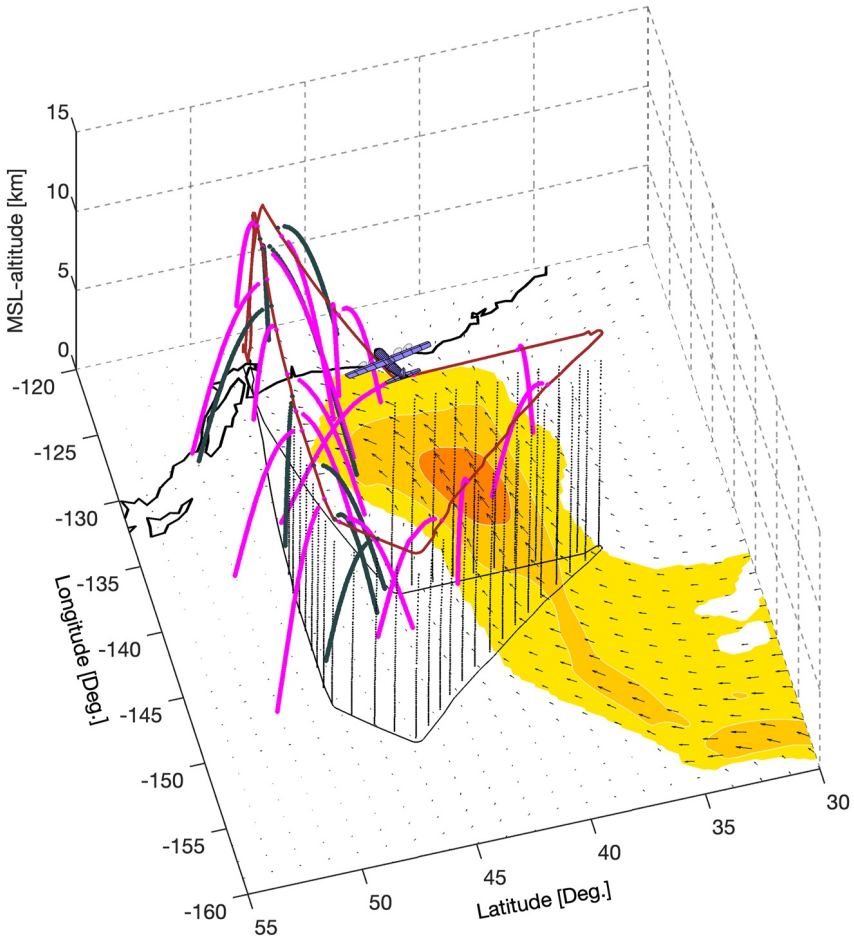

Figure 3. Three-dimensional view of the sampling by Airborne radio occultation (ARO) and dropsondes. Dark gray and magenta curves are the drifting tangent points from Galileo and Global Positioning System (GPS) occultations, respectively, and vertical black lines are dropsondes released from the aircraft. The aircraft trajectory is denoted by the brown line. Integrated water vapor transport (IVT) is indicated by contours on the lower surface. Also see Figure S1 and Movie S1 in Supporting Information S1.

3. AR Recon 2018 Measurement Campaign

The AR Recon 2018 field program ran from January 23 to March 15, 2018, targeting landfalling ARs that were forecast to impact the PACUS region. The demonstration case study presented here occurred on January 26 and 27, 2018.

3.1. Synoptic Situation

The landfalling AR that was the focus of the first Intensive Observing Period of 2018 (IOP1) developed rapidly following the breakdown of the subtropical ridge of high pressure in the northeastern Pacific and the associated anticyclone off the coast of California over January 25–28 (Figure 1). As an extratropical cyclone developed north of Hawaii, an associated AR developed that was limited in spatial extent but produced IVT exceeding 1,000 kg m^{-1} s^{-1}, making it an "extreme" intensity AR based on the AR Scale (Ralph et al., 2019). Here IVT is defined as the product of the specific humidity and horizontal wind at a given height and then integrated over height from the surface to 300 hPa (Neiman, Ralph, Wick, Lundquist, & Dettinger, 2008). By 00 UTC January 26, the AR had reached its characteristic dimensions (Ralph et al., 2017) of ~3,500 km long and 800–1,000 km wide at the 250 kg m^{-1} s^{-1} level. Uncertainty in the position and intensity of the aforementioned anticyclone led to considerable uncertainty in the location and intensity of the AR at landfall. By 00 UTC January 27, the extratropical cyclone evolved into a mesolow with pressure of 1,002 hPa about

1,000 km off the coast of Oregon while the anticyclone had moved southeastward with its center just off the coast of central California. The AR was located in the region of strong pressure gradient between these two features with IVT of 800 kg m^{-1} s^{-1}. This water vapor transport had reduced to 500 kg m^{-1} s^{-1} during landfall in Oregon by 12 UTC January 27 (not shown). To the north, a second larger extratropical cyclone in the Gulf of Alaska deepened further than anticipated to 966 hPa and water vapor transport of more than 1,000 kg m^{-1} s^{-1} impacted Vancouver, BC, Canada starting at approximately 00 UTC January 29 (not shown). These two pulses of IVT led to 3-day accumulated precipitation of more than 25 cm in Vancouver.

The sampling targets for the aircraft were guided by the location of steep gradients in water vapor within the AR, upper-level dynamics, and estimates of model forecast sensitivity. The Naval Research Laboratory Coupled Ocean-Atmosphere Mesoscale Prediction System (COAMPS) adjoint calculation of sensitivity (Doyle et al., 2014; Reynolds et al., 2019) for the 12-h accumulated precipitation in the Pacific Northwest from 00 to 12 UTC on January 27, indicated a region of high sensitivity to specific humidity at 500 hPa concentrated on the northern flank of the AR (Figure 2a). The forecast sensitivity to potential vorticity (PV) at 500 hPa (Figure 2b) was strongest north of the tail of the AR, with a broader region of lower amplitude PV sensitivity extending from about −150° to −135°E, between the AR and the extratropical cyclone center in the Gulf of Alaska. These sensitivities in the middle troposphere are most relevant for ARO as they are at the levels where the current configuration of this observing system has the highest accuracy. In the lower troposphere, strong sensitivity to specific humidity (Figure 2c) and potential temperature (Figure 2d) at 850 hPa were located at the eastern and western flanks of the AR.

3.2. IOP1 Research Flight

The National Oceanic and Atmospheric Administration (NOAA) G-IV aircraft flew out of Seattle, WA, to transect the AR and sample an anomaly in upper-level potential vorticity between the AR and the larger scale parent extratropical cyclone in the Gulf of Alaska during IOP1 from 18 UTC on January 26 to 04 UTC on January 27, 2018 (Figure 2). The flight was planned so that the dropsondes spanned within ±3 hr of 00 UTC and would be available for assimilation in the operational analyses for 00 UTC produced by NCEP and the ECMWF. The G-IV released dropsondes from a flight level of ∼13 km, sampling the upper-level atmospheric structure in the cold sector, and two transects across the AR. An additional Air Force C-130 based in Sacramento, CA, released dropsondes from a flight level of ∼10 km in the core of the AR and the mesolow that was responsible for accelerating the IVT toward the coast, to sample water vapor and winds in cross sections traversing the prefrontal low-level jet. A second Air Force C-130 based in Honolulu, HI, released dropsondes from a flight level of ∼10 km over the second pulse of IVT associated with a mesoscale frontal wave, and the region of high sensitivity to PV at the tail of the AR. Each aircraft also collected in situ flight level meteorological data, which on the NOAA G-IV was also used in the ARO data analysis.

We deployed a GNSS ARO system on the G-IV aircraft that included the high-accuracy Applanix POS/AV GPS inertial navigation system from GISMOS (Garrison et al., 2007; Murphy et al., 2015) operating at 10 Hz to achieve the optimal velocity precision of better than 5 mm/s for the airborne retrievals (Muradyan, 2012; Muradyan et al., 2010; Xie et al., 2008). The error in determining the aircraft velocity, is one factor in the accuracy of the retrieved ARO. Based on an analysis of the GISMOS system (Muradyan et al., 2011) the position accuracy determined for instrumentation deployed on the NOAA G-IV aircraft is better than 30 cm rms, and the velocity accuracy is 5 mm/s. For perspective, this is larger than the velocity accuracy of LEO spacecraft, and thus introduces refractivity errors in the retrieval that are larger than those for LEO RO at the top of the profile. Based on end-to-end refractivity retrieval simulations this leads to a refractivity standard deviation (std) of 0.5% at 11 km (Muradyan et al., 2011). At 11 km, 0.5% refractivity error corresponds to 1 K temperature error (Xie et al., 2008).

We deployed two next-generation dual-frequency Multi-GNSS phase locked loop tracking receivers to sample the cold sector and mid-to-upper levels in the AR. The receivers have an internal sampling rate of 100 Hz which is sufficient to track the phase accurately for relatively low expected atmospheric Doppler variations of ∼6 Hz (Wang et al., 2016, 2017) in the absence atmospheric multipath, which limits the ability to track into the lowest troposphere. The full GISMOS open-loop tracking system is anticipated to be available for future deployments to facilitate sampling lower levels, but was not operating in this campaign.

One receiver was a Septentrio POLARXS5 dual-frequency GNSS receiver (hereafter referred to as SEPT) and the other was a lightweight receiver package developed at Scripps Institution of Oceanography for flights on stratospheric superpressure balloons (Haase et al., 2018) using a multi-GNSS internal Septentrio AsterX4 OEM board (referred to as ROC2). Both are capable of tracking all GNSS constellations including Galileo, GPS, and the Russian GLONASS. They were connected to a Sensor Systems GPS-only L1/L2 avionics antenna on the top of the aircraft and sampled at 10 Hz. Because of the overlap in frequency bands between the Galileo and GPS constellations, Galileo signals were successfully tracked from the antenna, but not GLONASS.

3.3. ARO Profiling Observations

The sampling characteristics of the ARO observations are illustrated in Figure 3. The tangent points drift horizontally away from the aircraft as altitude decreases for a setting satellite, and the reverse for a rising satellite. The atmosphere is most dense at the tangent point, therefore the measured refractive delays for a given raypath are most strongly influenced by the atmospheric properties at that point. The retrieved values are representative of the refractivity, temperature and water vapor within roughly ± 90 km of the tangent point based on an estimate of the vertical resolution from the diameter of the first Fresnel zone and an approximate relation between horizontal and vertical resolution (Kursinski et al., 1997) or ±150 km based on the distance to accumulate 50% of the excess phase (Figures S2 and S3 in Supporting Information S1). The ARO profiles are distributed to both sides of the aircraft and the tangent point drift extends as far as 300 km from the aircraft flight path.

The two GNSS receivers provided two independent data sets to illustrate the ARO system performance, instrumental noise, and the resulting profile retrieval error. We retrieved 4 rising and 13 setting occultations from GPS satellites for a total of 17 out of the 35 possible occultations that could have theoretically been recorded based on the orbital geometry and aircraft trajectory at cruising altitude. We retrieved two rising and six setting occultations from Galileo out of a possible 12. These are the first profiles ever retrieved using signals from the Galileo constellation. The missing profiles were due to the satellite being too far forward or aft of the aircraft, or satellites not rising more than 10° above the horizon. This resulted in approximately three occultations per hour of flight time at cruising altitude (Figure 2), comparable to the typical rate of four dropsondes released per hour.

The receivers tracked an exceptionally large number of occultations, and tracked them low into the atmosphere compared to previous efforts with conventional receivers. Out of 25 occultations 18 sampled lower than 4 km altitude and one Galileo occultation sampled to the surface, near the core of the AR. On the second frequency, Galileo signals have significantly higher signal-to-noise ratio (SNR) than GPS signals, which helps in the signal tracking, and permits use of ionosphere corrected signals to lower penetration depth. The ARO observation data set is available at https://agsweb.ucsd.edu/airborne_ro.

Previous studies required open-loop tracking of GPS signals to reliably measure below 7 km (Haase et al., 2014; Murphy et al., 2015; Wang et al., 2017; Xie et al., 2008). The lower limit of the profile is strongly dependent on moisture gradients that typically produce large fluctuations in phase and amplitude due to atmospheric multipath that is best handled with open-loop tracking (Wang et al., 2017) that is not available routinely (Figure 4).

4. ARO Data Quality Assessment

4.1. Instrumental Error

The instrumental error is assessed based on the two independent data sets collected with two receivers. This captures differences due to random noise, principally due to thermal noise, residual clock errors, and unmodeled delays in the RF paths, and also illustrates discrepancies due to the eventual loss of lock at the lowest level of the profiles. In previous RO studies, because the independent observations were not exactly collocated, it was not possible to separate observation errors from differences due to atmospheric variability. Using multiple receivers, we assure the observations are exactly collocated, so that the differences should be considered the minimum observational error.

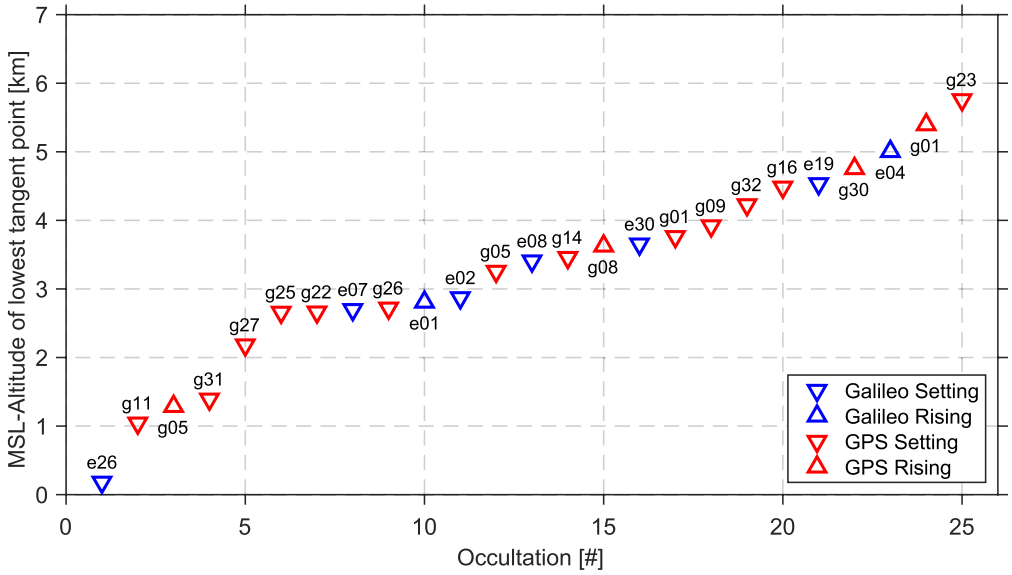

Figure 4. Altitude of the lowest point of each airborne radio occultation profile from the Global Positioning System (GPS, red triangles) and Galileo (blue triangles) constellations. Upward triangles are rising occultations and downward triangles are setting occultations. Profile e26 reached the surface.

To illustrate the size of the instrumental errors relative to variability of the atmosphere, we calculate the refractivity anomaly by subtracting the monthly zonal background refractivity profile (CIRAQ; Kirchengast et al., 1999) at 43°N as a reference. Figure 5 shows a comparison of occultations that were simultaneously measured by the ROC2 and SEPT receivers from the setting occultation of Galileo satellite e07s (blue solid and dotted lines). The profiles resolve nearly identical variations with an accuracy of better than 0.6% at

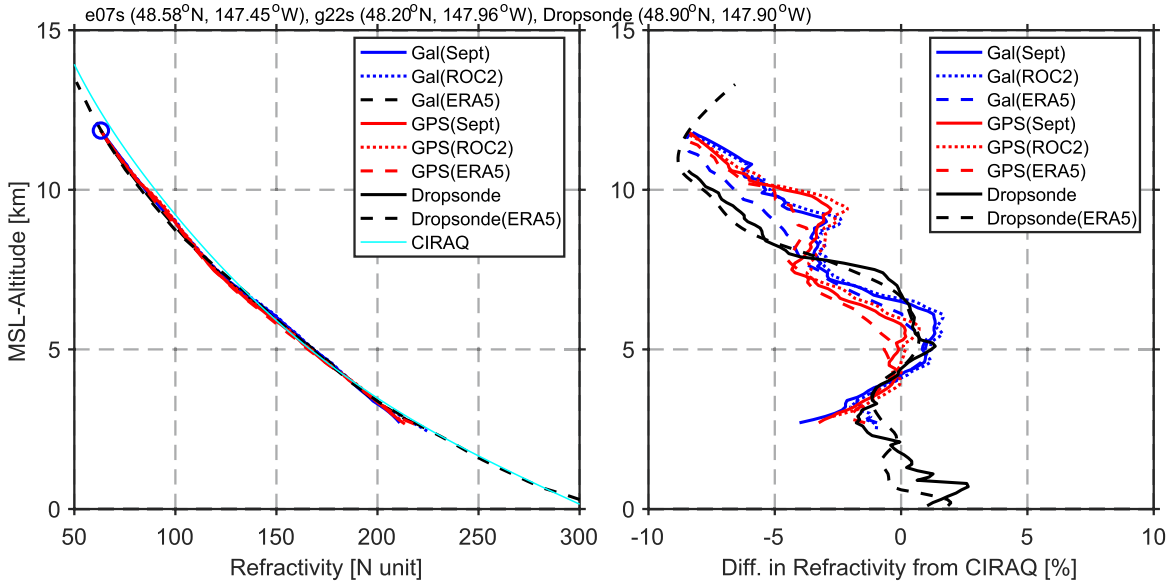

Figure 5. (a) Retrieved refractivity profiles sampling the warm sector from Global Positioning System (GPS) satellite g22s (red) and Galileo satellite e07s (blue) compared to the closest dropsonde (black) starting at the first quality-controlled value. Blue circle indicates the aircraft flight level data. ECMWF Reanalysis 5 (ERA5) reanalysis profiles extracted at the drifting tangent point locations of the GPS (red dashed) and the Galileo (blue dashed) occultations as well as the dropsonde (black dashed) are also shown. The cyan line indicates the CIRAQ climatological model. (b) Same as in (a) except for the refractivity anomaly, which is defined as the percent refractivity differences from the CIRAQ climatological model. Blue and red dotted lines show profiles derived from the ROC2 receiver, blue and red solid lines show profiles derived from the redundant SEPT receiver on the same flight.

vertical scales of less than 400 m. The same quality and resolution are also seen for the GPS occultation g22s (red solid and dotted lines), also recorded with both receivers.

These two occultations were selected because of their proximity (Figure 2) and show the quality that is typical of all retrieved profiles. Occultations g22s and e07s are 56 km apart at the top tangent point. The two profiles show very similar vertical structure with relative maxima in the refractivity anomaly at about 9.5 and 6 km height. The consistency of the heights of these layers is about 300 meters in the two profiles, and the difference in peak refractivity anomaly at those levels is a maximum of 1.5%. We attribute variability between 0.6% and 1.5% to fine scale variations in the troposphere over the small but significant geographic separation between the two profiles. Overall, the shape of the GPS and Galileo profiles is remarkably similar.

4.2. Comparisons With Dropsondes

Theoretical estimates of error sources have been modeled for airborne (Xie et al., 2008) and spaceborne systems (Kursinski et al., 1997). Statistical properties of ARO profiles have been studied for conventional (Murphy et al., 2015) and open-loop tracking receiver systems (Wang et al., 2016, 2017) using dropsonde, radiosonde and model analyses for comparisons. Dropsonde and radiosonde comparisons in previous studies in tropical regions yielded typical standard deviation of 2% refractivity difference compared to ARO, from about 4 km to flight level.

The dense dropsonde sampling of AR Recon allows a unique opportunity to evaluate the observation quality in the AR setting. The comparison of the ARO profiles with the dropsondes that are closest to the top tangent points are shown in Figure 5 in black. Within the layer with peak refractivity anomaly (∼6 km), the refractivity calculated from the dropsonde agrees with the two ARO profiles within 1.5%. The difference with the dropsonde is the same order as the consistency of the GPS and Galileo ARO profiles below 7 km. At the flight level, the ARO profiles are constrained by the in situ data so are close to the dropsonde values, but there is a larger difference above 8 km between the ARO profiles and the dropsonde, that we hypothesize is due to temperature gradients on the southern side of the flight track. The ARO profiles deviate from the dropsonde from 2.5 to 3 km height where the ARO receivers lose track of the signal. The ROC2 and SEPT profiles for the Galileo occultation also diverge at this height, setting the lower limit on the reliability of this profile. A rapid decrease of 15 dB in SNR occurs at the time when the tangent point reaches 3.0 km just before the receivers lose lock on the signal. The limit is much lower than previously published results using a tracking receiver (Murphy et al., 2015), primarily due to improvements in receiver and tracking technology.

Based on these comparisons and published estimates of accuracy, we summarize the characteristics of ARO observations in Table 1. We also provide estimates of the accuracy of dropsondes/radiosondes and LEO RO. From the many estimates of LEO RO accuracy in the UT/LS, such as the study of Anthes et al. (2008), we can conclude that it is more accurate than ARO. That study compares colocated COSMIC-1 satellite profiles and gives a refractivity precision of 0.2% from 8 to 20 km. Lower precision for ARO has been calculated given the effect of platform velocity errors in the upper troposphere, with decreasing impact in the lower troposphere where the error is smaller relative to the atmospheric Doppler (Xie et al., 2008). In the troposphere, the colocated LEO RO differences increases from std of 0.2%–1% at 2 km, where the raypaths can deviate significantly. This can be compared to the estimate of precision derived above for ARO from measurements of the differences between the multiple receiver comparison of colocated GPS and Galileo differences of 0.6%–1.5%.

For the purpose of this work where dropsondes are the key technique to sample the vertical profile within the highly variable features of the AR, it is useful to provide a measurement of RO accuracy based on comparisons with dropsondes and radiosondes. The difference is a useful measure of the accuracy with which RO represents the atmosphere at an in situ sounding point location. Some of this difference is due to horizontal atmospheric variability and part to the horizontal averaging length scale of the RO observation. (Ho et al., 2010) estimated differences between radiosonde and COSMIC-1 RO observations of retrieved moisture of about 1.5 g/kg std dev relative to radiosondes at 2 km height, using collocation criteria within 2 hr and 300 km, but did not calculate refractivity differences. However, COSMIC-2 has been well studied (Ho, Zhou, et al., 2020) and contributes a significant number of profiles between 30°N and 45°N. From 8 to 20 km, the refractivity std between radiosondes and LEO RO is 1% and the refractivity std increases from

Table 1
Characteristics of Dropsonde/Radiosonde, ARO, and LEO RO Observations in the AR Domain

Description	Accuracy/Precision	Resolution
AR Recon Dropsondes (RD94)/Radiosondes		
Measures Pressure (P), temperature (T), wind (u, v), and relative humidity (RH) Derived geopotential height (H) Platform: (NOAA Aircraft Observation Center G-IV aircraft) Domain: Pacific Ocean ARs ~30°latitude × 50° longitude ~8 h flights over ~15° × 15°	Precision: Hock and Franklin (1999) and Wang et al. (2015) P: 0.1 hPa T: 0.1 K q: 0.1% u, v: 0.2 m s^{-1} Accuracy: P: 0.5 hPa T: 0.2 Kq: 2% u,v: 0.5 m s^{-1}	Typical spatial sampling 90 km. Typical temporal sampling 6 min Typical 25 profiles per flight. Typical horizontal drift 15–25 km. P range: ~300–1,000 hPa Height range: 0 km to flight level (degraded q quality near flight level) Vertical sampling: ~1–2 hPa; 5–10 m Typically thinned to ~30 hPa; 150–300 m
Airborne Radio Occultation		
Measures excess phase due to atmospheric refractive index. Derived bending angle, refractivity, pressure, temperature, specific humidity, geometric height. Platform: (NOAA Aircraft Operations Center G-IV aircraft) Domain: Pacific Ocean ARs ~30°latitude × 50°longitude ~8 h flights over ~25°× 25° Limitations: w/o OL tracking has degraded quality and quantity in the lower troposphere. Negative bias in lowest 2 km[a]	Precision based on collocated observations: N: 0.6% @ 3–12 km T: 1.5 K @ 3–12 km q: ~10–20% @ 3–8 km Accuracy wrt Dropsondes: N: 1.8% @ 3–12 km T: 4K @ 3–12 km q: 30% @ 3–8 km	Typical spatial sampling 195 km (120 km minimum) Typical temporal sampling ~15 min (9 min minimum) Typical 25 profiles per flight (2018 GPS + Galileo) Typical 45 profiles per flight (2021 GPS + Galileo + Glonass) Typical horizontal drift: 350–400 km Height range (without OL tracking)[a]: ~3–~13 km flight level (>50% of profiles) Vertical sampling: 100 m First Fresnel zone vertical resolution: 600 m Corresponding horizontal resolution: ±90 to 150 km of tangent point
Spaceborne LEO RO		
Measures excess phase from atmospheric refractive index Derived bending angle, refractivity, pressure, temperature, specific humidity Platform: e.g., COSMIC-1, COSMIC-2 Domain: Global: 7 soundings per day per 5° × 5° latitude box (2018) ~9 soundings per day (2021) Limitations: Negative bias in lowest 1 km.	Precision based on collocated observations: (Anthes et al., 2008) N: 0.2% @ 8–20 km T: 0.5 K from 8 to 20 km N: 1%–0.2% @ 2–8 km T: 2.5–0.5 K @ 2–8 km q: 10% @ 2–8 km Accuracy wrt Dropsondes: Ho, Zhou, et al. (2020) and Sun et al. (2010) N: 1% @ 8–30 km T: 1.8 K @ 8–30 km N: 5.5%–1% @ 2–8 km; (COSMIC-2) N: 3%–1% @2–8 km; (COSMIC-1) T: 10 to 1.8 K @ 2–8 km q: 2–0.5 g/kg @ 2–8 km	Typical spatial sampling 1,500–2,000 km apart inside AR domain Typical temporal sampling ~1 h inside AR domain. Typical 3–6 profiles/6 hr inside AR domain (2018) Typical 9–10 profiles/6 hr inside AR domain (2020) Horizontal drift in lowest 10 km: 160 km. Height range ~2–60 km Vertical sampling: 100m Vertical sampling: 20–30 m 1st Fresnel zone resolution: 1.4 km Corresponding horizontal resolution: ±95 to 135 km of tangent point

[a]See Wang et al. (2017) for ARO with open-loop tracking.

1% at 8 km to 5.5% at 2 km (Figure 12 in Ho, Zhou, et al., 2020). We do not consider the LEO RO data below 2 km due to large refractivity biases below that height. These comparisons yield temperature differences of 1.7 K standard deviation, and specific humidity standard deviation from 0.5 g/kg at 8 km to 1.8 g/kg at 2 km.

We have made an estimate of accuracy for ARO based on the comparison with dropsondes and found a std dev of refractivity of 1.8% over the height range from 3 to 12 km (Table 1; Text S4 and Table S1 in the Supporting Information S1). This is significantly lower than the 5.5% difference seen in LEO RO profiles in lower levels globally (Ho, Zhou, et al., 2020) and what we find also in the north Pacific domain (Text S4 and Table S1 in the Supporting Information S1). An estimate of 1.8% atmospheric refractivity difference corresponds to 4 K temperature difference in this type of environment, and approximately 30% difference in specific humidity. The sampling characteristics and resolution of the three types of observations are also described in Table 1.

4.3. Comparison With Reanalysis

The ERA5 reanalysis product extracted at the dropsonde location is used to calculate the ERA5 refractivity anomaly profile shown in black dashed lines in Figure 5. The dropsonde data were assimilated into the ERA5 reanalysis, along with all operational observations, so the very close agreement within 1% over the height of the profile down to about 2 km is not surprising. For each ARO profile, we have extracted the required variables from the ERA5 product at each tangent point location to calculate refractivity, shown in blue dashed (e07s) and red dashed (g22s) lines. The variations in the dashed lines, for example, at 10 km, illustrate the horizontal variability of the ERA5 product within the close distance of the three observations. The agreement of ERA5 with the ARO profiles is close, but not as good as the agreement of ERA5 with the dropsondes, which could be attributed at least partially to the fact that the ARO data were not assimilated into the ERA5. The ARO observations at 10 km confirm that the ERA5 refractivity at this location is more than 1%–3% greater than at the dropsonde location, implying that the temperature is more than 2°–6° colder, assuming negligible water vapor at this height. The dropsonde and ARO observations illustrate that variations in tropopause structure in the AR environment are significant and dense sampling provides great benefits for resolving these variations.

The discrepancy between the ERA5 profiles and the ARO profiles, and to some extent the dropsondes, underscores possible model errors and/or biases near the tropopause. The Integrated Forecast System (IFS) that was used to generate ERA5 (Hersbach et al., 2020) may not resolve stratospheric intrusions well (e.g., Dyroff et al., 2015; Skerlak et al., 2015; Sprenger et al., 2003) that are typically associated with cold fronts (Keyser & Shapiro, 1986; Wernli et al., 2002). The ERA5 data were reported to have a large cold bias in the lower stratosphere and a small warm bias just below the tropopause when compared with the sounding data (Hersbach et al., 2020; Simmons et al., 2020). This pattern arises from the bias corrections of radiosonde and aircraft observations that are sensitive to the choice of the static climatological background-error covariance matrix (Simmons et al., 2020). COSMIC and other LEO RO data improved the cold bias in the lower stratosphere over the past two decades through the direct impact from assimilating RO data and the indirect anchoring impact on radiance data assimilation (Cucurull et al., 2014; Horanyi, 2017; Simmons et al., 2020). In this case, there are very few LEO RO observations in the area of thick clouds associated with the AR, so the discrepancy could be also due to assimilation of radiance that has not been well bias-corrected. ARO could provide additional anchoring for radiance bias corrections for such cases. The microphysics parameterization could be another cause of error. The IFS model was found to underestimate low clouds and overestimate high clouds (Ahlgrimm & Forbes, 2014; Jakob, 1999). The new physical parameterization in IFS (Ahlgrimm & Forbes, 2014; Joos & Forbes, 2016) has improved the boundary layer cloud representation, nevertheless, its influence on high clouds and temperature biases near the tropopause are worth further investigation with existing and new observations. ARO data could contribute to identifying key model deficiencies and systematic biases in the AR-related data-gapped areas (Zheng et al., 2021) over the North Pacific Ocean. Despite being a reliable and unique data set, exact agreement between ARO and unbiased reanalysis data is not expected because of the horizontal resolution of the ARO observations and their representation of horizontal variability.

4.4. Horizontal Gradients in Atmospheric Structure

The main motivation to make simultaneous observations with ARO and dropsondes is to capture the variations in structure in the AR and the frontal zone in a broader area around the flight track. The dropsondes and ARO sample different volumes within the AR. Figure 6 shows the temperature at a height of 7 km from a high-resolution mesoscale model run, which will be described in more detail in the following section. Along the northernmost segment of the flight track where the dropsondes sample, there is a strong gradient

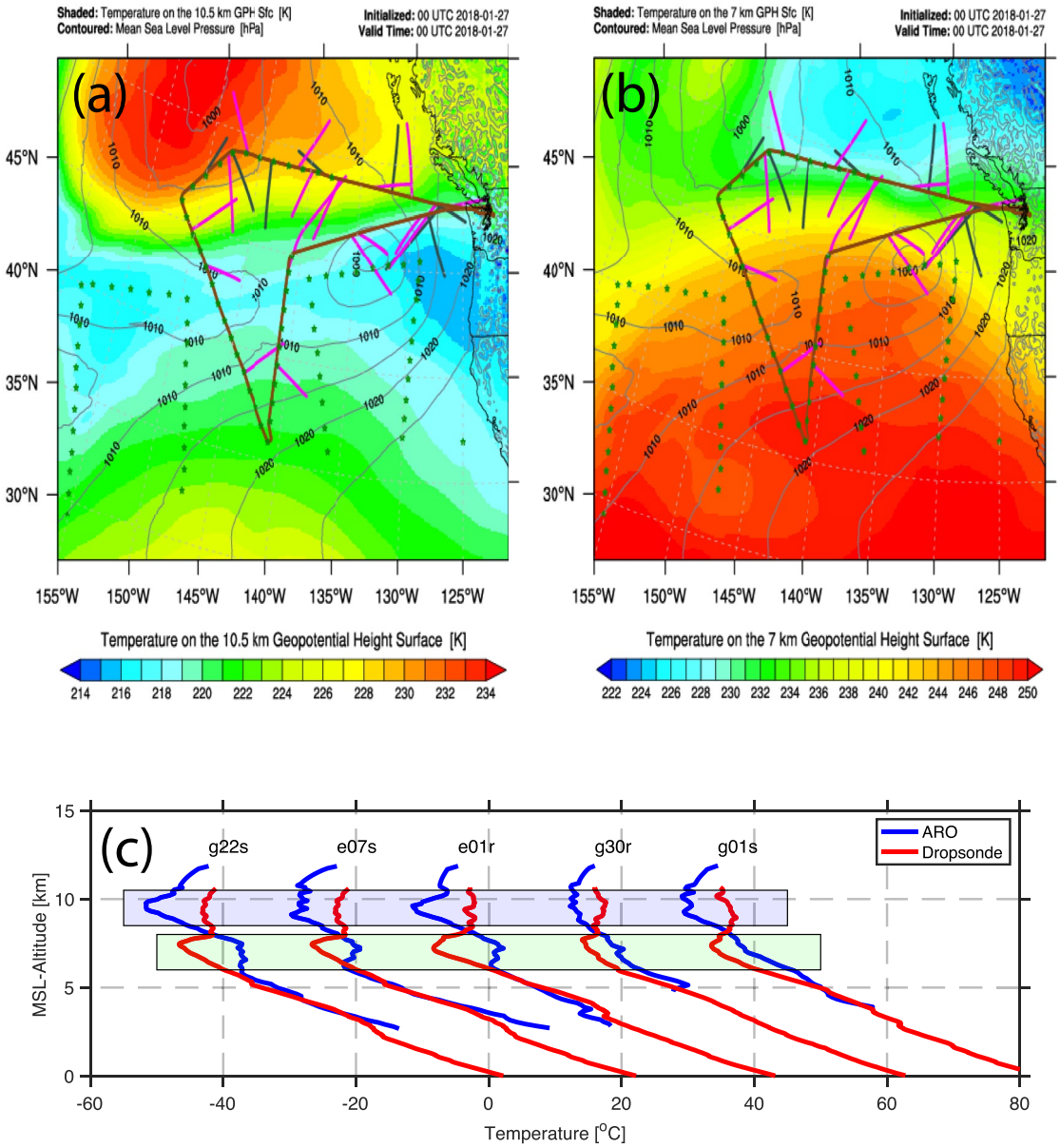

Figure 6. Horizontal temperature variations associated with tropopause structure are captured by the airborne radio occultation (ARO) and dropsonde profiles. (b) Temperature at 7 km height, from a mesoscale model analysis at 00UTC January 26, 2018. Temperature increases toward the south on the south side of the northern flight leg that is sampled by five occultations. (a) Temperature at 10.5 km height decreases toward the south. (c) ARO profiles (blue) that sample south of the dropsondes are systematically cooler at 10.5 km and warmer at 7 km than the dropsonde profiles, in agreement with the general temperature gradient. Profile locations are labeled in Figure 2a, and the refractivity structure from g22s and e07s are also discussed in Figure 5.

between colder temperatures to the north and warmer temperature to the south where the five ARO profiles shown in Figure 6 sample.

At 10.5 km, the gradient is reversed with warmer temperatures on the north side, which is a result of a much higher and colder tropopause in the south. The five ARO temperature profiles sampling the south side of the flight track show colder temperatures at 10.5 km and warmer temperatures at 7 km compared to the volume of air sampled by the dropsondes beneath the track, consistent with the mesoscale model temperature gradients. These first-order variations in the midupper-level troposphere are clearly seen in the differences between ARO and dropsondes. Figure 3 gives a good view of the horizontal sampling of ARO, predominantly outside the AR because of the targeting objective of the G-IV of the upper-level potential

vorticity in the frontal zone. Figure 6 illustrates how large the temperature variations are that sensed by the complementary techniques over this horizontal scale. It suggests that horizontal variability contributes to the differences in refractivity seen in the intercomparison of data sets in Figure 5.

5. Data Assimilation Increments to the Mesoscale Model Produced by ARO

The previous sections illustrated that the ARO observations resolve significant vertical variations in atmospheric structure similar to the dropsonde observations, and the number of profiles is comparable, but they do not often reach the surface. They do not provide the detailed horizontal resolution of dropsondes, nor do they provide wind measurements. However, because the retrieved quantity, refractivity, is a simple function of temperature and water vapor, we hypothesize that the type of impact on water vapor and temperature in the midlevels will be similar to that of dropsondes. Therefore, we investigate how the model distributes that impact into areas not sampled by dropsondes.

5.1. Experiment Design

The spatial impact of the observations was investigated in numerical experiments utilizing the WRF model (Skamarock et al., 2008). The Advanced Research WRF dynamical core of WRF version 4.1.1 was employed, which is a fully compressible, Euler nonhydrostatic model with terrain following hydrostatic pressure vertical coordinates. The model configuration was based on the operational West-WRF model running at the CW3E (Martin et al., 2018). We implemented the model on a two-way nested grid with 27 and 9 km resolution and corresponding mesh sizes of 355 × 300 elements and 799 × 661 elements. The model top was set at 10 hPa with 48 computational layers. The Grell-Freitas convection (Grell & Freitas, 2014), Unified NOAH land surface model (Livneh et al., 2010), Thompson double-moment physics (Thompson et al., 2008), Yonsei University (YSU) planetary boundary layer (Hong & Pan, 1996), and the Rapid Radiative Transfer Model for Global Circulation Models (RRTMG) longwave and shortwave (Iacono et al., 2008; Mlawer et al., 1997) parameterizations were used.

We used three-dimensional variational (3DVAR) data assimilation in the WRF Data Assimilation (WRFDA) system (also version 4.1.1) (Barker et al., 2012), which relies on a static background-error (BE) covariance for determining the spatial correlation of the model increments. The major advantages of the 3DVAR method are the low computational cost and the ability to assimilate refractivity directly, rather than retrieved temperature and water vapor (Chen et al., 2018). The background-error covariance for each layer of the model was calculated from the differences between 24 and 12-hr WRF forecasts initialized every 12 h over a period of 1 month, from January 15 to February 15, 2018, using the NMC method (Parrish & Derber, 1992), the aforementioned model setup, and the GENBE version 1.0 utility (Barker et al., 2004) with BE Covariance option 5. The localization of the analysis increment was adjusted for the winds only, based on a single observation test (Descombes et al., 2015), to be approximately 500 km for both u and v wind speed at 700 hPa.

The numerical experiments were initialized at 18:00 UTC January 26, 2018 using the analysis from the control member of the NCEP Global Ensemble Forecast System (GEFS). The WRF model was then run forward for 6 hr, using the GEFS control member forecast as boundary conditions, to allow the effects of downscaling the coarser resolution GEFS to be brought into balance. The resulting 6-hr forecast valid at 00:00 UTC January 27, 2018 serves as the "No DA" experiment, which is an estimate of the atmospheric state for comparison with the assimilation results and also the background (first guess) state on which data assimilation is performed on the outermost (27 km) grid. The four DA experiments assimilate each of the following types of data individually: (a) only the radiosonde and dropsonde observations contained in the operational NCEP prepbufr file, (b) only the ARO refractivity from the GPS constellation, (c) the ARO refractivity from the GPS and Galileo constellations, and (d) only refractivity from operational spaceborne RO platforms. The spaceborne RO data set includes all satellites that are assimilated operationally in the NCEP Global Data Assimilation System (GDAS), which at the time only included signals sent from the GPS constellation. Only those observations that were made within a 6-hr time window from 21:00 UTC January 26, 2018 to 03:00 UTC the following day were used for data assimilation in these numerical experiments.

A relatively simple observation operator that approximates Equation 1 (Zou et al., 1995) was used for the assimilation of the RO observations within the data assimilation package, as in many of the initial RO

data assimilation studies (Cucurull et al., 2006; Healy et al., 2005). This operator was updated to take into account that the value of refractivity at each point in a given RO profile is at the geographic location of the tangent point (the point closest to the surface of the Earth along the ray) that drifts horizontally, as illustrated in Figure 3 (Chen et al., 2018). Each tangent point is treated as an independent measurement, therefore the horizontal drift in a given observed RO profile is represented within the data assimilation algorithm, regardless of whether the occultation was collected from a receiver aboard a spaceborne or airborne platform. The model covariance extends the increment horizontally in the region of the observed tangent point. By incorporating tangent point drift in the operator, the increment will be displaced horizontally at different heights. The additional spreading of the information horizontally due to the tangent point drift is not large, except for exceptionally large tangent point drifts which can happen during aircraft turns (Chen et al., 2018). The use of a local operator for refractivity neglects variations of refractivity along the raypath, which could contribute an equivalent error of 2% to the retrieved refractivity for a raypath crossing perpendicular to a cold front (Xie et al., 2008). In previous studies that compare different approaches, the use of a simpler operator resulted in an underestimation of the magnitude of the increment (Chen et al., 2018), so we expect the resulting increments in this case may also be an underestimate.

The observation error used for ARO is the same as that for spaceborne RO in WRFDA. We base this on error estimates from collocated dropsonde comparisons, which provide insight into how well RO represents the refractivity of the atmosphere at a point location, useful when using the refractivity operator (Figure S10 and Table S1 in Supporting Information S1). Estimates on the order of 1%–2% in the lower troposphere are reasonable first-order assumptions based on end-to-end error simulations carried out in Xie et al. (2008). The error is assigned by an algorithm within WRFDA that uses the height and latitude of a given tangent point to specify a profile of observation error that varies from approximately 2% in the lower troposphere to 0.3% near the tropopause, closely following observation errors for local operators used in previous studies (e.g., Chen et al., 2009).

5.2. Data Assimilation Results

The refractivity assimilation produces temperature and moisture increments to be added to the background first guess model fields to better fit the new observations. Because the refractivity depends also on pressure, there are small increments in the wind field as well. The new analysis, at 00 UTC 27 January 2018, serves as the initial conditions for the ensuing forecast for the precipitation at landfall.

In the sounding data assimilation experiment (Figure 7a), there are no significant increments to the humidity on the north leg of the G-IV flight track, and a positive increment (higher humidity) is found near the northwest corner near the cold front. The remainder of the area has a negative increment (lower humidity), mainly in the region of the AR and warm sector. There are very small anticyclonic and cyclonic wind increments as might be expected, associated with the moisture increments, and several regions where the wind increment is coherent and of larger spatial extent. The GPS-only ARO moisture increment (Figure 7c), shows a positive (higher humidity) change in an area in the center of the flight track that is not sampled by the dropsondes. To the east of each of the southern three legs of the G-IV track, the moisture increment is negative. The ARO data have the effect of spreading the increment into the space between the different flight tracks (Figure S2 in Supporting Information S1), consistent with the spatial pattern in the dropsonde increments. The GPS + Galileo ARO moisture increment (Figure 7d), shows a very similar pattern with larger amplitude. This indicates overall consistency between GPS and Galileo, as was illustrated in Figure 5, and also promises even more impact as the number of profiles increases with the future use of the GLONASS satellites.

We also show the results assimilating the very sparsely available operational LEO satellite RO data (Figure 7d), for the most part outside the AR. In the entire model, domain that included most of the Pacific Ocean and North America, we used all 42 LEO RO observations from all constellations included in the NCEP GDAS in the 6 hr data assimilation window, however there were only six LEO RO observations in the region of interest shown in Figure 7d. This is not always the case, but in general it is unlikely to find many LEO RO observations concentrated within the relatively compact region of the AR, even considering the new COSMIC-2 constellation which does not sample midlatitudes well. The forecast impact on the accumulated precipitation (Figure S3 in Supporting Information S1) relative to the NO DA experiment is

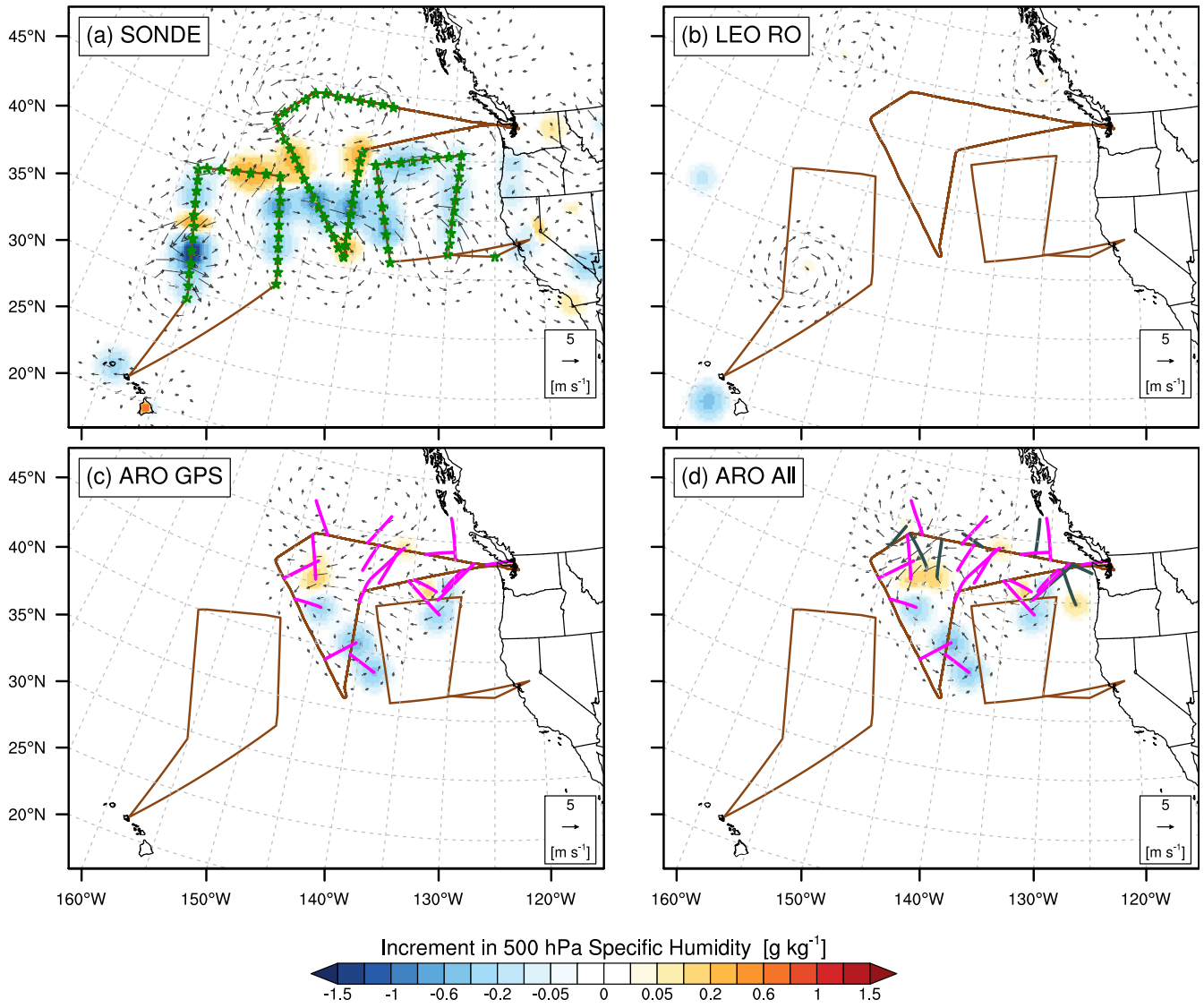

Figure 7. (a) Weather Research and Forecasting (WRF) analysis increment in 500 hPa moisture at 00 UTC January 27, 2018 after assimilation of dropsondes and radiosondes (locations indicated by green stars), (b) Low Earth Orbiting (LEO) RO observations (tangent points not shown), (c) Airborne radio occultation (ARO) observations from Global Positioning System (GPS) only (tangent points indicated by pink lines), and (d) ARO observations from GPS + Galileo (tangent points indicated by pink and dark gray lines).

similar for the soundings and ARO GPS + Galileo, indicating that both data sets are trending toward greater precipitation over Vancouver Island. Our primary conclusion is that the impact of the ARO data produces adjustments of the model first guess in the correct directions as cross validated by the dropsonde impact and usefully extends that impact into otherwise unobserved areas. Full data denial experiments replicating an operational observation system, which are beyond the scope of this work, would be necessary to fully assess the added value of data sets collected via ARO.

We calculated the mean and standard deviation of the differences between the ARO observations and the mesoscale model and also the ERA5 reanalysis (Figure S4 in Supporting Information S1). The mean and standard deviation were smaller for the mesoscale WRF model runs with and without the dropsondes assimilated than the ERA5 above 5 km, suggesting that downscaling the global analysis product increased the accuracy as well as assimilating dropsondes, using the independent ARO observations as an objective measure in the region above 5 km where they are most accurate. Thus, the independent ARO observations

can also be useful for validation of analysis and forecast products, thereby contributing to the broader forecasting improvement objectives.

6. Discussion

6.1. Vertical Structure of the Atmospheric River

The classic vertical structure of an AR (Ralph et al., 2017; American Meteorological Society Glossary of Meteorology) derived from a composite of dropsonde transects of 21 AR events, has a moist low-level jet in advance of the cold front carrying the vast majority of the horizontal water vapor transport. The mid-latitude jet stream is found above the frontal zone, equatorward of the region of tropopause folding. We calculated cross sections of the atmospheric refractivity from the WRF experiments to illustrate the impacts of the ARO data on the midlevel moisture at the top of the AR core. In midlevels instability may lead to the initiation of convection and latent heat release that is hypothesized to intensify the associated extratropical cyclone (Berman & Torn, 2019; Demirdjian et al., 2020; Zhang et al., 2019), which may have played a role in the deepening of the cyclone on the day following the flight in this case (Figure 1). Because refractivity varies exponentially with height, similar to density, we subtract the CIRAQ monthly zonal climatological average refractivity profile (Kirchengast et al., 1999) appropriate for the local latitude (42°N) to highlight the vertical and horizontal variations in the refractivity anomaly. The use of the monthly zonal climatology presents the anomaly in a way that is insensitive to the current longitudinal position of the AR which is evolving in time, and provides a reference that permits the refractivity anomaly to be interpreted generally with respect to any other AR.

Figure 8 shows the refractivity anomaly cross sections through the WRF model experiment that assimilated ARO data, along the line parallel to the western-most G-IV flight across the AR indicated in Figure 2. The cross section is offset 3° longitude to the east of the flight track in order to cross the area sampled by the ARO observations. Potential temperature is shown in gray contour lines, and the thick dashed line indicates the dynamic tropopause, defined here by the 2 PVU contour (Browning & Roberts, 1994; Hoskins et al., 1985).

The core of the AR shows up as a high refractivity anomaly (due to the water vapor dominant term in the equation for N) sloping upwards over the cold front, following very closely the classical representation of an AR, which is superimposed without modification of scale for illustrative purposes (Ralph et al., 2017). Dry air appears as a low N anomaly behind the cold front, creating a sharp boundary layer below 1 km. There is a transition in the sign of the N anomaly at 9 km, because the refractivity Equation 1 contains a temperature dependent term that dominates above 9 km and a water vapor dependent term that dominates below 9 km (Murphy et al., 2015).

In the upper levels, the fractional change in N is the opposite of the fractional change in temperature, so high N implies colder temperatures (red shading). The high N (cold) in the south and low N (warm) in the north is typical of a baroclinic system and of a sloping tropopause that is higher toward the south, as was noted in Figure 6. However, the dynamic tropopause contour (dashed black) also highlights a tropopause fold poleward of the upper-level front, a feature that is common near the jet stream because of the ageostrophic circulation at the jet entrance, and often produces deep intrusions of stratospheric air and potential vorticity into the troposphere (Danielsen, 1968; Hoskins et al., 1985).

This refractivity anomaly is a new way of representing AR structure, which provides additional insight and illustrates how the assimilation of the ARO data that is sensitive to the vertical structure provides direct constraints on the features produced by the mesoscale model. The ARO experiment increment (Figure 8b) shows that the ARO observations amplify the contrast of the low-level moisture that is lifted along the cold front in comparison to the drier air above, which is one way to discriminate diabatically active regions. An increase in moisture increment (higher refractivity) is present where the dynamic tropopause contour extends to lower levels. The negative refractivity increment in the upper-level jet stream core indicates warmer temperatures there. The slanting structure of the moist AR with height is clear in the ARO experiment and is also enhanced in the DROPS experiment compared to NoDA (Figure S5 in Supporting Information S1).

Previous work attempted to elucidate the vertical structure of an offshore AR directly from an approximately linear transect of 12 COSMIC RO profiles occurring on the same day (Neiman, Ralph, Wick, Kuo,

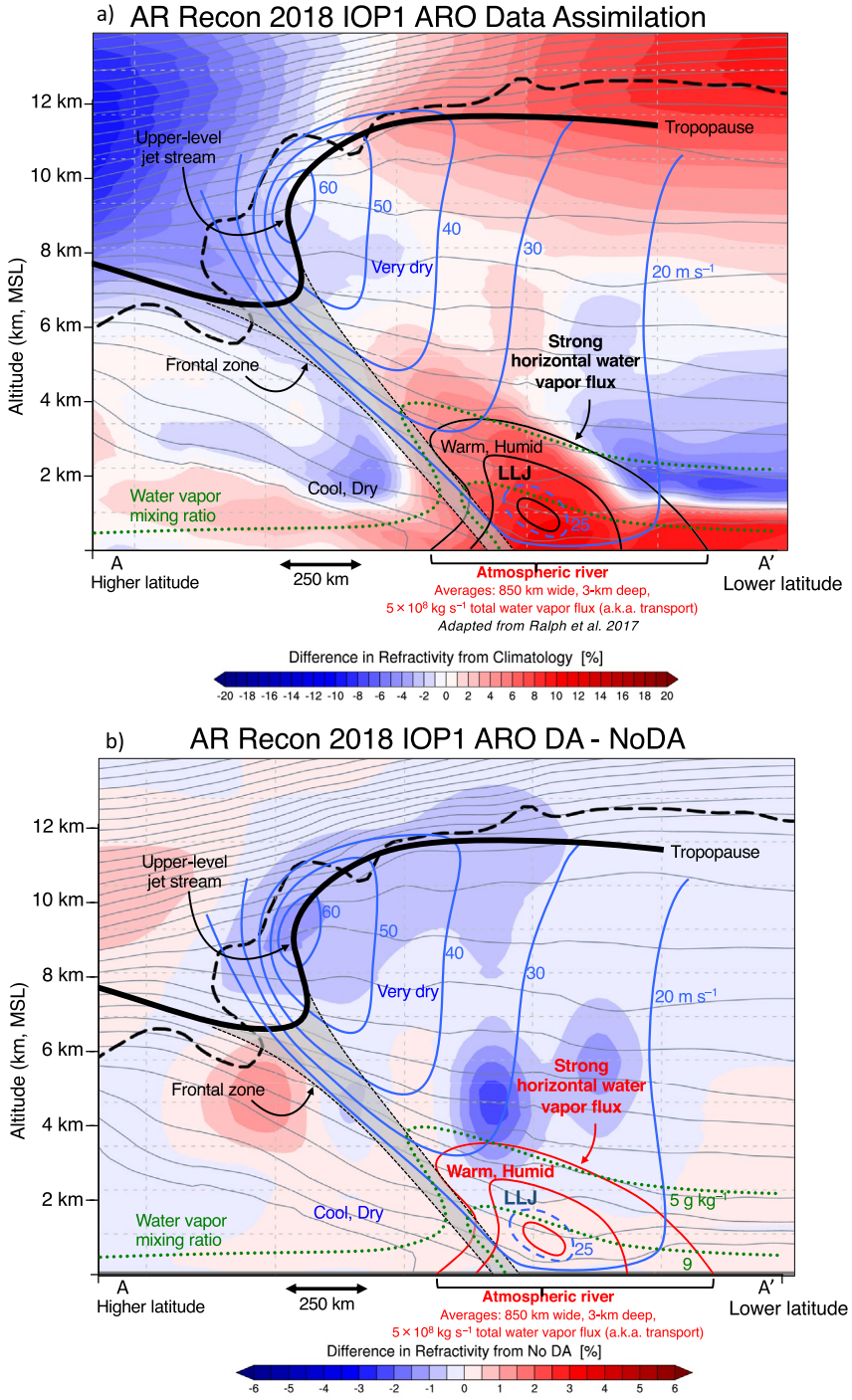

Figure 8. (a) Refractivity anomaly cross section through the Weather Research and Forecasting (WRF) model airborne radio occultation (ARO) experiment. This transect is taken along the black dashed line indicated in Figure 2a, which is parallel to the western transect across the atmospheric river (AR) but offset 3° to the east of the flight track in order to cross the area sampled by ARO. Refractivity anomaly (shaded, %) is the difference from a climatological model. The dynamic tropopause (2 PVU contour) from the model is represented by the thick black dashed line. Potential temperature contours are shown in gray. The schematic representation of the vertical structure of the AR (Ralph et al., 2017) with schematic contours for wind speed (blue) integrated water vapor transport (black/red) and mixing ratio (green) is superimposed on the refractivity anomaly, with no adjustments to the horizontal or vertical scale. (b) Same as (a) but for the difference in refractivity between the ARO and NoDA experiments.

et al., 2008). It captured the sloping polar cold front in the potential temperature contours and a band of enhanced specific humidity near the surface coinciding with the peak value of IVT. However, the shape of the structures was difficult to discern given the sparsity of the profiles. Data assimilation of refractivity at each individual tangent point of the profiles is the approach that we took to provide continuous refractivity fields, similar to Ma et al. (2011), rather than creating a composite as in (Neiman, Ralph, Wick, Kuo, et al., 2008). In addition, we focus on interpretation of the refractivity anomaly. This captures in one parameter the key features of the AR, both those controlled by temperature and by moisture. Extending the concept proposed in the COSMIC study, the cross section through the continuous refractivity field shows the shape of the AR as it ascends over the cold front, and captures the dry air behind the cold front, the warm air intrusion in the tropopause fold, and the variations in boundary layer thickness and sharpness in all regions. Figure 8 is useful also to illustrate the difficulty in capturing AR characteristics with separate composites on the cold side, the core, and the warm side of the AR. For example, grouping all profiles on the cold side to create a composite profile removes sharp contrasts when ignoring the sloping structure. Composites of integrated vapor transport have difficulty reproducing sharp horizontal gradients when integrating vertically across the sloping AR structure. Compositing across multiple ARs without knowledge of where the sloping structures are also removes the sharp contrasts. It would be informative to create refractivity anomaly transects directly from the RO observations with enhanced density, beyond what was possible in the 2008 study. The dense midlatitude sampling of LEO RO profiles has suffered from the demise of the COSMIC-1 constellation, and COSMIC-2 satellites in tropical orbits do not adequately cover midlatitude ARs. However, we hope that eventually combining the observation density of ARO with enhanced open-loop tracking with new commercial LEO missions will make it possible to create transects directly from the observations. Even with the limitation that the integrating nature of the observations would reduce the sharp contrasts across fronts for raypaths traversing perpendicular to the front (Xie et al., 2008), with enough observations we anticipate that the horizontal variability at the scale illustrated in Figure 8 could be elucidated. In this case, working with refractivity anomaly removes the concern about dependence of the retrievals on first guess models and makes it clear how any missing RO observations near the surface affect the interpretation.

The final point to emphasize is that this perspective provides insight for potentially improving the observational capabilities of LEO RO. The general view that RO capabilities are reduced in high moisture environments is common in the literature and has been attributed to atmospheric multipath due to sharp moisture gradients, especially in the tropics. However, there has not been a careful study of the cause. Also common are examples of superrefraction in the boundary layer that prevent sampling to the surface. Zheng et al. (2021) has described the existence of a data gap inside ARs where radiance observations are lower quality and vertically sparse, and indicated also fewer LEO RO profiles are available. While this is true, there are observations of ARO and LEO RO profiles reaching the surface in the water vapor maximum of the AR core (Murphy et al., 2020). Here we provide some explanation for the cause.

The ARO signals on either side of the AR core can be valuable for indicating the lowest extent of dry air at the top of the marine boundary layer, revealing variations in stability across the AR. Where the water vapor in the frontal zone extends from the surface to the midlevels, for example, within the core of an AR, a representative vertical profile is saturated and vertical refractivity gradients are smoother, and therefore the RO signal passing through this region produces smooth variations in phase as the rays get closer to the Earth's surface. However, on the poleward side of the frontal zone, cold dry air overlies moist air in the boundary layer creating a very sharp refractivity gradient. An RO signal passing through this region will vary smoothly in excess phase, until the rays reach that boundary layer where superrefraction is likely to occur and interrupt signal tracking.

On the equatorward side of the frontal zone, the gradient between midlevel drier air and the saturated moist air near the ocean surface gradually increases, for example, far enough away from the southern edge of the AR core, the gradients would also be expected to be strong enough to produce superrefraction at the top of the boundary layer. The key points are that there is a substantially wide zone of moisture sloping upwards over the cold front where RO signals are likely to be able to penetrate, and these data can inform models of the potential for diabatic heating and production of PV (Browning & Roberts, 1994; Kuo et al., 1991). The sensitivity of precipitation forecasts to perturbations in water vapor was generally found in the moist inflow and ascent regions near the junction of the warm and cold fronts, within the northern flank of an

AR (Reynolds et al., 2019). Similarly, rapidly developing extratropical cyclones in the Atlantic Ocean basin are sensitive to the ascent of filaments of low-level moisture (Doyle et al., 2014), particularly in this 3–6 km height range. The correlation of AR water vapor with intensifying extratropical cyclones has been documented in Zhang et al. (2019). In a very recent paper Zhang and Ralph (2021) found that cyclogenesis events that occurred with an AR in its nascent warm sector deepened 50% faster on average than cyclones without an AR in its initial environment, a key result that further indicates the details of AR-related parameters, and of IVT itself, offshore when trying to predict cyclogenesis and its impacts. Therefore, successful RO observations in the core of the AR could be very valuable.

6.2. Prospects for Future Operational Measurements

Currently the ARO profiles collected on a reconnaissance flight are postprocessed after the flight has landed. If rapid orbit and clock products are used, the ARO profiles from these receivers potentially could be calculated in near real time, which would be crucial for real-time assimilation of ARO data at operational centers, and would facilitate data denial experiments with the full observational system. The ARO observations are being incorporated into data assimilation experiments for retrospective case studies to increase the midlevel coverage of high vertical resolution water vapor and temperature observations laterally offset from the aircraft tracks, beneath which the dropsonde data provide unique information. Their potential contribution to understanding AR-enhanced adiabatic processes amplifying cyclogenesis (Demirdjian et al., 2020; Doyle et al., 2014; Reynolds et al., 2019; Zhang & Ralph, 2021; Zhang et al., 2019) can be evaluated from a multiseason extended data set. These additional independent observations are also useful for independent validation of analysis and forecast products, thereby contributing to the broader forecasting improvement objectives.

Currently, the observations as shown in Figure 4, do not always extend low enough to sample the AR core. We have demonstrated in the hurricane environment (Chen et al., 2018; Haase et al., 2014; Wang et al., 2017) that the GISMOS ARO system with open-loop tracking and the phase matching bending angle retrieval technique can sample near the surface. We are currently carrying out experiments with a GNSS signal recorder on the NOAA aircraft to enable that technology in the future for ARs.

7. Conclusions

We evaluated the accuracy of Global Navigation Satellite System airborne radio occultation (ARO) observations through multiple intercomparisons. We retrieved the first Galileo RO profiles, which provided a very closely spaced comparison of multiple ARO profiles to illustrate the reliability of the measurements despite large tangent point drift in a highly three-dimensional frontal system. The profiles agreed within 1% and showed highly correlated vertical structure at about 400 m resolution. We operated two receiver systems onboard the aircraft to retrieve occultations with identical propagation paths that showed the repeatability of refractivity observations to be an approximately constant 0.5% N with height. Of the 25 occultations retrieved in the 8-hr flight, 11 sampled lower than 3 km. We compared the retrieved ARO profiles to the closest dropsonde observations, released from the same aircraft, a unique accomplishment enabled by the collaboration with NOAA and CW3E. These showed similar vertical structure and variations consistent with the horizontal structure of the baroclinic frontal system reproduced in the mesoscale numerical model. In comparisons with the ECMWF ERA5 reanalysis product extracted at the location of the drifting tangent points, the standard deviation of the differences was less than 2% in refractivity above 4 km.

ARO observations complement dropsonde observations beneath the aircraft in reconnaissance missions by sampling the area in the environment to the sides of the flight track and enhancing the three-dimensional representation of the environmental temperature and water vapor over a broader geographical area than would otherwise be observed. This is important in atmospheric rivers where dense clouds and heavy precipitation limit the full exploitation of satellite radiances. Additionally, ARO profiles and dropsondes have the potential to identify significant model biases that may be associated with cloud-affected satellite radiances. ARO observations were compared to an experiment that assimilated dropsonde data and showed reduced biases in the 7–12 km height range, relative to the case where ARO observations were compared to ERA5. We showed that over the vertical extent of the ARO profiles, the analysis increment in moisture was

comparable in spatial scale to dropsondes and filled in areas between and around the exterior of the flight tracks that were not sampled. While the data assimilation tests for one case study do not provide statistical evidence of impact on the precipitation, the tests motivate implementation of a systematic operational data collection effort to enable full data denial experiments in high-resolution models. This data set adds significantly to the Atmospheric Rivers Reconnaissance Program targeted observation system designed to address the 1–5 days lead time forecasting objectives for improved prediction of flooding and water management in the PACUS region. Including ARO measurements leverages the investment in the National Winter Season Operations Plan aircraft. While dropsondes provide the most accurate measurements of AR temperature and moisture, and importantly include winds, ARO can supplement these flight data significantly over a limited vertical range by more than doubling the number of aircraft soundings, collecting profiles over the entire flight without additional expendable costs, and providing the capability to collect data inside or adjacent to airspace where dropsondes are not permitted.

Our last remark is that LEO RO has not been fully used to advantage in the troposphere, partly because of a lack of confidence in the capabilities of RO in high moisture weather systems and the highly variable three-dimensional nature of the atmosphere, compared to the stratosphere where the highest accuracy of LEO RO has been achieved. This study gives confidence in the prospects for exploiting LEO RO in the lower troposphere by showing the repeatability of the measurements. We also illustrate the potential for large gains in understanding of the moist processes in atmospheric rivers and associated frontal systems, since the features in the simulated refractivity field represented in Figure 8 are the native parameter sampled by the RO observations.

Data Availability Statement

The data are available at https://agsweb.ucsd.edu/airborne_ro/data/2018.023_ar2018/. The authors thank the three anonymous reviewers for the care and thoroughness of their reviews.

Acknowledgments
This work was supported by NSF Grant AGS-1642650 and AGS-1454125, NASA Grant NNX15AU19G. Support was also provided by the CW3E and the Atmospheric River Research Program of the California Department of Water Resources and the US Army Corps of Engineers Forecast-Informed Reservoir Operations Program. The authors would like to thank NSF & the NCAR EOL facility for the loan of the Applanix navigation system, A. Borsa for the Septentrio equipment loan, and D. Jabson for his assistance with the ROC equipment. Flights on the G-IV aircraft were provided by NOAA. The authors would like to acknowledge the assistance of the NOAA Aircraft Operations Center staff, in particular G. Defeo and J. Parrish. The authors would like to thank J. Doyle and C. Reynolds from NRL for providing the sensitivities from COAMPS. The authors thank CW3E staff, B. Kawzenuk and R. Demirdjian, for facilitating access to the CW3E dropsonde and other data. The authors thank S.-H. Chen (UC Davis) for useful discussions regarding the data assimilation and I. Sepulveda for contributing to a review of the article. Resources supporting this work were provided by the NASA High-End Computing (HEC) Program.

References

Ahlgrimm, M., & Forbes, R. (2014). Improving the representation of low clouds and drizzle in the ECMWF model based on ARM observations from the Azores. *Monthly Weather Review*, *142*(2), 668–685. https://doi.org/10.1175/mwr-d-13-00153.1

Ancell, B., & Hakim, G. J. (2007). Comparing adjoint- and ensemble-sensitivity analysis with applications to observation targeting. *Monthly Weather Review*, *135*(12), 4117–4134. https://doi.org/10.1175/2007mwr1904.1

Anthes, R. A., Bernhardt, P. A., Chen, Y., Cucurull, L., Dymond, K. F., Ector, D., et al. (2008). The COSMIC/FORMOSAT-3 Mission: Early results. *Bulletin of the American Meteorological Society*, *89*(3), 313–334. https://doi.org/10.1175/bams-89-3-313

Aparicio, J. M., & Deblonde, G. (2008). Impact of the assimilation of CHAMP refractivity profiles on Environment Canada global forecasts. *Monthly Weather Review*, *136*(1), 257–275. https://doi.org/10.1175/2007mwr1951.1

Barker, D., Huang, X.-Y., Liu, Z., Auligne, T., Zhang, X., Rugg, S., et al. (2012). The Weather Research and Forecasting model's community variational/ensemble data assimilation system WRFDA. *Bulletin of the American Meteorological Society*, *93*(6), 831–843. https://doi.org/10.1175/bams-d-11-00167.1

Barker, D. M., Huang, W., Guo, Y.-R., Bourgeois, A., & Xiao, Q. (2004). A three-dimensional variational data assimilation system for MM5: Implementation and initial results. *Monthly Weather Review*, *132*(4), 897–914. https://doi.org/10.1175/1520-0493(2004)132<0897:atvdas>2.0.co;2

Bauer, P., Radnoti, G., Healy, S., & Cardinali, C. (2014). GNSS radio occultation constellation observing system experiments. *Monthly Weather Review*, *142*(2), 555–572. https://doi.org/10.1175/mwr-d-13-00130.1

Berman, J. D., & Torn, R. D. (2019). The impact of initial condition and warm conveyor belt forecast uncertainty on variability in the downstream waveguide in an ECWMF case study. *Monthly Weather Review*, *147*(11), 4071–4089. https://doi.org/10.1175/mwr-d-18-0333.1

Browning, K. A., & Roberts, N. M. (1994). Structure of a frontal cyclone. *Quarterly Journal of the Royal Meteorological Society*, *120*(520), 1535–1557. https://doi.org/10.1002/qj.49712052006

Centurioni, L. R. (2018). Drifter technology and impacts for sea surface temperature, sea-level pressure, and ocean circulation studies. In R. Venkatesan, A. Tandon, E. Dasaro, & M. A. Atmanand (Eds.), *Observing the oceans in real time* (pp. 37–57). https://doi.org/10.1007/978-3-319-66493-4_3

Chen, S.-Y., Huang, C.-Y., Kuo, Y.-H., Guo, Y.-R., & Sokolovskiy, S. (2009). Assimilation of GPS refractivity from FORMOSAT-3/COSMIC using a nonlocal operator with WR 3DVAR and its impact on the prediction of a typhoon event. *Terrestrial, Atmospheric and Oceanic Sciences*, *20*, 133–154. https://doi.org/10.3319/tao.2007.11.29.01(f3c)

Chen, X. M., Chen, S. H., Haase, J. S., Murphy, B. J., Wang, K. N., Garrison, J. L., et al. (2018). The impact of airborne radio occultation observations on the simulation of Hurricane Karl (2010). *Monthly Weather Review*, *146*(1), 329–350. https://doi.org/10.1175/mwr-d-17-0001.1

Corringham, T. W., Ralph, F. M., Gershunov, A., Cayan, D. R., & Talbot, C. A. (2019). Atmospheric rivers drive flood damages in the western United States. *Science Advances*, *5*(12), eaax4631. https://doi.org/10.1126/sciadv.aax4631

Cucurull, L., Anthes, R. A., & Tsao, L. L. (2014). Radio occultation observations as anchor observations in numerical weather prediction models and associated reduction of bias corrections in microwave and infrared satellite observations. *Journal of Atmospheric and Oceanic Technology*, *31*(1), 20–32. https://doi.org/10.1175/jtech-d-13-00059.1

Cucurull, L., Derber, J. C., Treadon, R., & Purser, R. J. (2007). Assimilation of global positioning system radio occultation observations into NCEP's global data assimilation system. *Monthly Weather Review*, *135*(9), 3174–3193. https://doi.org/10.1175/mwr3461.1

Cucurull, L., Kuo, Y. H., Barker, D., & Rizvi, S. R. H. (2006). Assessing the impact of simulated COSMIC GPS radio occultation data on weather analysis over the Antarctic: A case study. *Monthly Weather Review*, *134*(11), 3283–3296. https://doi.org/10.1175/mwr3241.1

Danielsen, E. F. (1968). Stratospheric-tropospheric exchange based on radioactivity ozone and potential vorticity. *Journal of the Atmospheric Sciences*, *25*(3), 502–518. https://doi.org/10.1175/1520-0469(1968)025<0502:STEBOR>2.0.CO;2

Demirdjian, R., Doyle, J. D., Reynolds, C. A., Norris, J. R., Michaelis, A. C., & Ralph, F. M. (2020). A case study of the physical processes associated with the atmospheric river initial-condition sensitivity from an adjoint model. *Journal of the Atmospheric Sciences*, *77*(2), 691–709. https://doi.org/10.1175/jas-d-19-0155.1

Descombes, G., Auligné, T., Vandenberghe, F., Barker, D. M., & Barré, J. (2015). Generalized -sit covariance matrix model (GEN_BE v2. 0). *Geoscientific Model Development*, *8*(3), 669–696. https://doi.org/10.5194/gmd-8-669-2015

Dettinger, M. D., Ralph, F. M., Das, T., Neiman, P. J., & Cayan, D. R. (2011). Atmospheric rivers, floods and the water resources of California. *Water*, *3*(2), 445–478. https://doi.org/10.3390/w3020445

Doyle, J. D., Amerault, C., Reynolds, C. A., & Reinecke, P. A. (2014). Initial condition sensitivity and predictability of a severe extratropical cyclone using a moist adjoint. *Monthly Weather Review*, *142*(1), 320–342. https://doi.org/10.1175/mwr-d-13-00201.1

Dyroff, C., Zahn, A., Christner, E., Forbes, R., Tompkins, A. M., & van Velthoven, P. F. J. (2015). Comparison of ECMWF analysis and forecast humidity data with CARIBIC upper troposphere and lower stratosphere observations. *Quarterly Journal of the Royal Meteorological Society*, *141*(688), 833–844. https://doi.org/10.1002/qj.2400

Garrison, J. L., Walker, M., Haase, J. S., Lulich, T., Xie, F., Ventre, B. D., et al. (2007). Development and testing of the GISMOS instrument. In *Proceedings of the IEEE International Geoscience and Remote Sensing Symposium* (pp. 5105–5108). IEEE. https://doi.org/10.1109/igarss.2007.4424010

Grell, G. A., & Freitas, S. R. (2014). A scale and aerosol aware stochastic convective parameterization for weather and air quality modeling. *Atmospheric Chemistry and Physics*, *14*(10), 5233–5250. https://doi.org/10.5194/acp-14-5233-2014

Haase, J. S., Alexander, M. J., Hertzog, A., Kalnajs, L., Deshler, T., Davis, S. M., et al. (2018). Around the world in 84 day—Strateole-2 investigates the tropical atmosphere with long duration superpressure balloons. *EOS*, *99*. https://doi.org/10.1029/2018eo091907

Haase, J. S., Murphy, B. J., Muradyan, P., Nievinski, F., Larson, K. M., Garrison, J. L., & Wang, K.-N. (2014). First results from an airborne GPS radio occultation system for atmospheric profiling. *Geophysical Research Letters*, *40*, 1759–1765. https://doi.org/10.1002/2013GL058681

Healy, S. B. (2013). Surface pressure information retrieved from GPS radio occultation measurements. *Quarterly Journal of the Royal Meteorological Society*, *139*(677), 2108–2118. https://doi.org/10.1002/qj.2090

Healy, S. B., Haase, J., & Lesne, O. (2002). Abel transform inversion of radio occultation measurements made with a receiver inside the Earth's atmosphere. *Annales Geophysicae*, *20*(8), 1253–1256. https://doi.org/10.5194/angeo-20-1253-2002

Healy, S. B., Jupp, A. M., & Marquardt, C. (2005). Forecast impact experiment with GPS radio occultation measurements. *Journal of Geophysical Research*, *32*, L03804. https://doi.org/10.01029/02004GL020806

Healy, S. B., & Thepaut, J. N. (2006). Assimilation experiments with CHAMP GPS radio occultation measurements. *Quarterly Journal of the Royal Meteorological Society*, *132*(615), 605–623. https://doi.org/10.1256/qj.04.182

Hersbach, H., Bell, B., Berrisford, P., Hirahara, S., Horanyi, A., Munoz-Sabater, J., et al. (2020). The ERA5 global reanalysis. *Quarterly Journal of the Royal Meteorological Society*, *146*(730), 1999–2049. https://doi.org/10.1002/qj.3803

Ho, S.-P., Anthes, R. A., Ao, C. O., Healy, S., Horanyi, A., Hunt, D., et al. (2020). The COSMIC/FORMOSAT-3 radio occultation mission after 12 years: Accomplishments, remaining challenges, and potential impacts of COSMIC-2. *Bulletin of the American Meteorological Society*, *101*, E1107–E1136. https://doi.org/10.1175/BAMS-D-18-0290.1

Ho, S. P., Zhou, X. J., Kuo, Y. H., Hunt, D., & Wang, J. H. (2010). Global evaluation of radiosonde water vapor systematic biases using GPS radio occultation from COSMIC and ECMWF analysis. *Remote Sensing*, *2*(5), 1320–1330. https://doi.org/10.3390/rs2051320

Ho, S. P., Zhou, X. J., Shao, X., Zhang, B., Adhikari, L., Kireev, S., et al. (2020). Initial assessment of the COSMIC-2/FORMOSAT-7 neutral atmosphere data quality in NESDIS/STAR using in situ and satellite data. *Remote Sensing*, *12*(24), 4099. https://doi.org/10.3390/rs12244099

Hock, T. F., & Franklin, J. L. (1999). The NCAR GPS dropwindsonde. *Bulletin of the American Meteorological Society*, *80*(3), 407–420. https://doi.org/10.1175/1520-0477(1999)080<0407:TNGD>2.0.CO;2

Hong, S. Y., & Pan, H. L. (1996). Nonlocal boundary layer vertical diffusion in a medium-range forecast model. *Monthly Weather Review*, *124*(10), 2322–2339. https://doi.org/10.1175/1520-0493(1996)124<2322:NBLVDI>2.0.CO;2

Horanyi, A. (2017). Some aspects on the use and impact of observations in the ERA5 Copernicus Climate Change Service reanalysis. *Idojaras*, *121*(4), 329–344.

Horanyi, A., Cardinali, C., & Centurioni, L. (2017). The global numerical weather prediction impact of mean-sea-level pressure observations from drifting buoys. *Quarterly Journal of the Royal Meteorological Society*, *143*(703), 974–985. https://doi.org/10.1002/qj.2981

Hoskins, B. J., McIntyre, M. E., & Robertson, A. W. (1985). On the use and significance of isentropic potential vorticity maps. *Quarterly Journal of the Royal Meteorological Society*, *111*(470), 877–946.

Iacono, M. J., Delamere, J. S., Mlawer, E. J., Shephard, M. W., Clough, S. A., & Collins, W. D. (2008). Radiative forcing by long-lived greenhouse gases: Calculations with the AER radiative transfer models. *Journal of Geophysical Research*, *113*, D13103. https://doi.org/10.1029/2008JD009944

Jakob, C. (1999). Cloud cover in the ECMWF reanalysis. *Journal of Climate*, *12*(4), 947–959. https://doi.org/10.1175/1520-0442(1999)012<0947:cciter>2.0.co;2

Joos, H., & Forbes, R. M. (2016). Impact of different IFS microphysics on a warm conveyor belt and the downstream flow evolution. *Quarterly Journal of the Royal Meteorological Society*, *142*(700), 2727–2739. https://doi.org/10.1002/qj.2863

Keyser, D., & Shapiro, M. A. (1986). A review of the structure and dynamics of upper-level frontal zones. *Monthly Weather Review*, *114*(2), 452–499. https://doi.org/10.1175/1520-0493(1986)114<0452:AROTSA>2.0.CO;2

Kirchengast, G., Hafner, J., & Poetzi, W. (1999). *The CIRA86aQ_UoG model: An extension of the CIRA-86 monthly tables including humidity tables and a Fortran95 global moist air climatology model*.

Kuo, Y. H., Reed, R. J., & Lownam, S. (1991). Effects of surface-energy fluxes during the early development and rapid intensification stages of 7 explosive cyclones in the western Atlantic. *Monthly Weather Review*, *119*(2), 457–476. https://doi.org/10.1175/1520-0493(1991)119<0457:eosefd>2.0.co;2

Kursinski, E. R., Hajj, G. A., Hardy, K. R., Schofield, J. T., & Linfield, R. (1997). Observing Earth's atmosphere with radio occultation measurements. *Journal of Geophysical Research*, *102*(23), 23429–23465. https://doi.org/10.1029/97JD01569

Lesne, O., Haase, J., Kirchengast, G., Ramsauer, J., & Poetzi, W. (2002). Sensitivity analysis for airborne sounding of the troposphere by GNSS radio occultation. *Physics and Chemistry of the Earth*, *27*(4–5), 291–299. https://doi.org/10.1016/s1474-7065(02)00003-7

Livneh, B., Xia, Y., Mitchell, K. E., Ek, M. B., & Lettenmaier, D. P. (2010). Noah LSM snow model diagnostics and enhancements. *Journal of Hydrometeorology*, *11*(3), 721–738. https://doi.org/10.1175/2009jhm1174.1

Ma, Z., Kuo, Y.-H., Ralph, F. M., Neiman, P. J., Wick, G. A., Sukovich, E., & Wang, B. (2011). Assimilation of GPS radio occultation data for an intense atmospheric river with the NCEP regional GSI system. *Monthly Weather Review*, *139*(7), 2170–2183. https://doi.org/10.1175/2011mwr3342.1

Ma, Z. Z., Kuo, Y. H., Wang, B., Wu, W. S., & Sokolovskiy, S. (2009). Comparison of local and nonlocal observation operators for the assimilation of GPS RO data with the NCEP GSI system: An OSSE study. *Monthly Weather Review*, *137*(10), 3575–3587. https://doi.org/10.1175/2009mwr2809.1

Majumdar, S. J. (2016). A review of targeted observations. *Bulletin of the American Meteorological Society*, *97*(12), 2287–2303. https://doi.org/10.1175/bams-d-14-00259.1

Majumdar, S. J., Sellwood, K. J., Hodyss, D., Toth, Z., & Song, Y. C. (2010). Characteristics of target areas selected by the ensemble transform Kalman filter for medium-range forecasts of high-impact winter weather. *Monthly Weather Review*, *138*(7), 2803–2824. https://doi.org/10.1175/2010mwr3106.1

Martin, A., Ralph, F. M., Demirdjian, R., DeHaan, L., Weihs, R., Helly, J., et al. (2018). Evaluation of atmospheric river predictions by the WRF model using aircraft and regional mesonet observations of orographic precipitation and its forcing. *Journal of Hydrometeorology*, *19*(7), 1097–1113. https://doi.org/10.1175/jhm-d-17-0098.1

Martin, A. C., Ralph, F. M., Wilson, A., DeHaan, L., & Kawzenuk, B. (2019). Rapid cyclogenesis from a mesoscale frontal wave on an atmospheric river: Impacts on forecast skill and predictability during atmospheric river landfall. *Journal of Hydrometeorology*, *20*(9), 1779–1794. https://doi.org/10.1175/JHM-D-18-0239.1

Mlawer, E. J., Taubman, S. J., Brown, P. D., Iacono, M. J., & Clough, S. A. (1997). Radiative transfer for inhomogeneous atmospheres: RRTM, a validated correlated-k model for the longwave. *Journal of Geophysical Research*, *102*(D14), 16663–16682. https://doi.org/10.1029/97JD00237

Muradyan, P. (2012). *Profiling the atmosphere with the airborne GPS radio occultation technique using open-loop tracking (PhD thesis)*. Purdue University.

Muradyan, P., Haase, J. S., Xie, F., Garrison, J. L., Lulich, T., & Voo, J. (2010). GPS/INS navigation precision and its effect on airborne radio occultation retrieval accuracy. *GPS Solutions*, *15*, 207–218. https://doi.org/10.1007/s10291-010-0183-7

Muradyan, P., Haase, J. S., Xie, F., Garrison, J. L., Lulich, T., & Voo, J. (2011). GPS/INS navigation precision and its effect on airborne radio occultation retrieval accuracy. *GPS Solutions*, *15*, 207–218 https://doi.org/10.1007/s10291-010-0183-7

Murphy, B. J., Haase, J. S., Muradyan, P., Garrison, J. L., & Wang, K.-N. (2015). Airborne GPS radio occultation refractivity profiles observed in tropical storm environments. *Journal of Geophysical Research*, *120*, 1690–1709. https://doi.org/10.1002/2014JD022931

Murphy, M. J., Jr, Haase, J. S., Cao, B., Ralph, F. M., & Hordyniec, P. (2020). Evaluation of commercial and public GNSS RO observations during the atmospheric river reconnaissance campaigns. Paper presented at the American Geophysical Union Annual Meeting, San Francisco, CA, USA.

Neiman, P. J., Ralph, F. M., Wick, G. A., Kuo, Y. H., Wee, T. K., Ma, Z. Z., et al. (2008). Diagnosis of an intense atmospheric river impacting the Pacific Northwest: Storm summary and offshore vertical structure observed with COSMIC satellite retrievals. *Monthly Weather Review*, *136*(11), 4398–4420. https://doi.org/10.1175/2008mwr2550.1

Neiman, P. J., Ralph, F. M., Wick, G. A., Lundquist, J. D., & Dettinger, M. D. (2008). Meteorological characteristics and overland precipitation impacts of atmospheric rivers affecting the West Coast of North America based on eight years of SSM/I satellite observations. *Journal of Hydrometeorology*, *9*(1), 22–47. https://doi.org/10.1175/2007jhm855.1

OFCM. (2019). *National winter season operations plan*. (pp. 1–77). Office of the Federal Coordinator for Meteorology. Retrieved from https://www.icams-portal.gov/publications/nwsop/2019_nwsop.pdf

Parrish, D. F., & Derber, J. C. (1992). The National Meteorological Centers spectral statistical interpolation analysis system. *Monthly Weather Review*, *120*(8), 1747–1763. https://doi.org/10.1175/1520-0493(1992)120<1747:TNMCSS>2.0.CO;2

Poli, P., Moll, P., Puech, D., Rabier, F., & Healy, S. B. (2009). Quality control, error analysis, and impact assessment of FORMOSAT-3/COSMIC in numerical weather prediction. *Terrestrial, Atmospheric and Oceanic Sciences*, *20*(1), 101–113. https://doi.org/10.3319/tao.2008.01.21.02(f3c)

Ralph, F. M., Cannon, F., Tallapragada, V., Davis, C. A., Doyle, J. D., Pappenberger, F., et al. (2020). West coast forecast challenges and development of atmospheric river reconnaissance. *Bulletin of the American Meteorological Society*, *101*(8), E1357–E1377. https://doi.org/10.1175/bams-d-19-0183.1

Ralph, F. M., Coleman, T., Neiman, P. J., Zamora, R. J., & Dettinger, M. D. (2013). Observed impacts of duration and seasonality of atmospheric-river landfalls on soil moisture and runoff in Coastal Northern California. *Journal of Hydrometeorology*, *14*(2), 443–459. https://doi.org/10.1175/jhm-d-12-076.1

Ralph, F. M., Iacobellis, S. F., Neiman, P. J., Cordeira, J. M., Spackman, J. R., Waliser, D. E., et al. (2017). Dropsonde observations of total integrated water vapor transport within North Pacific Atmospheric Rivers. *Journal of Hydrometeorology*, *18*(9), 2577–2596. https://doi.org/10.1175/jhm-d-17-0036.1

Ralph, F. M., Neiman, P. J., & Wick, G. A. (2004). Satellite and CALJET aircraft observations of atmospheric rivers over the eastern north Pacific Ocean during the winter of 1997/98. *Monthly Weather Review*, *132*(7), 1721–1745. https://doi.org/10.1175/1520-0493(2004)132<1721:sacaoo>2.0.co;2

Ralph, F. M., Rutz, J. J., Cordeira, J. M., Dettinger, M., Anderson, M., Reynolds, D., et al. (2019). A scale to characterize the strength and impacts of atmospheric rivers. *Bulletin of the American Meteorological Society*, *100*(2), 269–289. https://doi.org/10.1175/bams-d-18-0023.1

Rennie, M. P. (2010). The impact of GPS radio occultation assimilation at the Met Office. *Quarterly Journal of the Royal Meteorological Society*, *136*(646), 116–131. https://doi.org/10.1002/qj.521

Reynolds, C. A., Doyle, J. D., Ralph, F. M., & Demirdjian, R. (2019). Adjoint sensitivity of North Pacific atmospheric river forecasts. *Monthly Weather Review*, *147*, 1871–1897. https://doi.org/10.1175/mwr-d-18-0347.1

Rüeger, J. (2002). *Refractive index formulae for electronic distance measurements with radio and millimetre waves (Unisurv Rep, 109)*.

Rutz, J. J., Steenburgh, W. J., & Ralph, F. M. (2014). Climatological characteristics of atmospheric rivers and their inland penetration over the Western United States. *Monthly Weather Review*, *142*(2), 905–921. https://doi.org/10.1175/mwr-d-13-00168.1

Schreiner, W. S., Weiss, J. P., Anthes, R. A., Braun, J., Chu, V., Fong, J., et al. (2020). COSMIC-2 radio occultation constellation: First results. *Geophysical Research Letters*, *47*, e2019GL086841. https://doi.org/10.1029/2019GL086841

Simmons, A., Soci, C., Nicolas, J., Bell, B., Berrisford, P., Dragani, R., et al. (2020). *Global stratospheric temperature bias and other stratospheric aspects of ERA5 and ERA5.1*. Retrieved from https://www.ecmwf.int/node/19362

Skamarock, W. C., Klemp, J. B., Dudhia, J., Gill, D. O., Barker, D. M., Wang, W., & Powers, J. G. (2008). A description of the Advanced Research WRF version 3 (NCAR Technical note-475+ STR).

Skerlak, B., Sprenger, M., Pfahl, S., Tyrlis, E., & Wernli, H. (2015). Tropopause folds in ERA-Interim: Global climatology and relation to extreme weather events. *Journal of Geophysical Research: Atmospheres*, *120*, 4860–4877. https://doi.org/10.1002/2014JD022787

Sprenger, M., Maspoli, M. C., & Wernli, H. (2003). Tropopause folds and cross-tropopause exchange: A global investigation based upon ECMWF analyses for the time period March 2000 to February 2001. *Journal of Geophysical Research*, *108*(D12), 8518. https://doi.org/10.1029/2002JD002587

Sun, B. M., Reale, A., Seidel, D. J., & Hunt, D. C. (2010). Comparing radiosonde and COSMIC atmospheric profile data to quantify differences among radiosonde types and the effects of imperfect collocation on comparison statistics. *Journal of Geophysical Research*, *115*, D23104. https://doi.org/10.1029/2010JD014457

Thompson, G., Field, P. R., Rasmussen, R. M., & Hall, W. D. (2008). Explicit forecasts of winter precipitation using an improved bulk microphysics scheme. Part II: Implementation of a new snow parameterization. *Monthly Weather Review*, *136*(12), 5095–5115. https://doi.org/10.1175/2008mwr2387.1

Torn, R. D., & Hakim, G. J. (2008). Ensemble-based sensitivity analysis. *Monthly Weather Review*, *136*(2), 663–677. https://doi.org/10.1175/2007mwr2132.1

Wang, J. H., Young, K., Hock, T., Lauritsen, D., Behringer, D., Black, M., et al. (2015). A long-term, high-quality, high-vertical-resolution GPS dropsonde dataset for hurricane and other studies. *Bulletin of the American Meteorological Society*, *96*(6), 961–973. https://doi.org/10.1175/bams-d-13-00203.1

Wang, K.-N., Garrison, J. L., Acikoz, U., Haase, J. S., Murphy, B. J., Muradyan, P., & Lulich, T. (2016). Open-loop tracking of rising and setting GNSS radio-occultation signals from an airborne platform: Signal model and error analysis. *IEEE Transactions on Geosciences and Remote Sensing*, *54*(7), 3967–3984. https://doi.org/10.1109/tgrs.2016.2532346

Wang, K.-N., Garrison, J. L., Haase, J. S., & Murphy, B. J. (2017). Improvements to GPS airborne radio occultation in the lower troposphere through implementation of the phase matching method. *Journal of Geophysical Research: Atmospheres*, *122*, 10–266. https://doi.org/10.1002/2017JD026568

Wernli, H., Dirren, S., Liniger, M. A., & Zillig, M. (2002). Dynamical aspects of the life cycle of the winter storm "Lothar" (24–26 December 1999). *Quarterly Journal of the Royal Meteorological Society*, *128*(580), 405–429. https://doi.org/10.1256/003590002321042036

Xie, F., Haase, J. S., & Syndergaard, S. (2008). Profiling the atmosphere using the airborne GPS radio occultation technique: A sensitivity study. *IEEE Transactions on Geoscience and Remote Sensing*, *46*(11), 3424–3435. https://doi.org/10.1109/tgrs.2008.2004713

Xie, F. Q., Adhikari, L., Haase, J. S., Murphy, B., Wang, K. N., & Garrison, J. L. (2018). Sensitivity of airborne radio occultation to tropospheric properties over ocean and land. *Atmospheric Measurement Techniques*, *11*(2), 763–780. https://doi.org/10.5194/amt-11-763-2018

Zhang, Z., & Ralph, F. M. (2021). The influence of antecedent atmospheric river conditions on extratropical cyclogenesis. *Monthly Weather Review*, *149*(5), 1337–1357. https://doi.org/10.1175/mwr-d-20-0212.1

Zhang, Z. H., Ralph, F. M., & Zheng, M. H. (2019). The relationship between extratropical cyclone strength and atmospheric river intensity and position. *Geophysical Research Letters*, *46*, 1814–1823. https://doi.org/10.1029/2018GL079071

Zheng, M. H., Delle Monache, L., Wu, X. R., Ralph, F. M., Cornuelle, B., Tallapragada, V., et al. (2021). Data gaps within atmospheric rivers over the Northeastern Pacific. *Bulletin of the American Meteorological Society*, *102*(3), E492–E524. https://doi.org/10.1175/bams-d-19-0287.1

Zhu, Y., & Newell, R. E. (1998). A proposed algorithm for moisture fluxes from atmospheric rivers. *Monthly Weather Review*, *126*(3), 725–735. https://doi.org/10.1175/1520-0493(1998)126<0725:APAFMF>2.0.CO;2

Zou, X., Kuo, Y. H., & Guo, Y. R. (1995). Assimilation of atmospheric radio refractivity using a nonhydrostatic adjoint model. *Monthly Weather Review*, *123*, 2229–2250. https://doi.org/10.1175/1520-0493(1995)123<2229:AOARRU>2.0.CO;2

Journal of Geophysical Research - Atmospheres

Supporting Information for

Multi-GNSS Airborne Radio Occultation Observations as a Complement to Dropsondes in Atmospheric River Reconnaissance

J. S. Haase[1], M.J. Murphy[1], B. Cao[1], F.M. Ralph[2], M. Zheng[2], L. Delle Monache[2]

[1] Scripps Institution of Oceanography, University of California San Diego, La Jolla, CA

[2] Center for Western Weather and Water Extremes, Scripps Institution of Oceanography, University of California San Diego, La Jolla, CA

Contents of this file

Additional Supporting Information (Files uploaded separately)

Introduction

In the airborne radio occultation (ARO) technique, similar to RO from low earth orbiting (LEO) satellites, nearly horizontally propagating radio waves arriving at the antenna from angles below the local horizon undergo significant refractive bending and a Doppler shift due to variations of the atmospheric refractive index at each level of the atmosphere through which the raypath passes. In the standard retrieval process, the integrated delay over a nearly horizontal raypath is reduced to a representative value of refractivity at the tangent point (point of closest approach of the raypath to the Earth) where the propagation delay is concentrated. The ARO retrieval technique is adapted to the slowly moving airborne geometry where the tangent point drifts horizontally during the occultation. This supporting information provides further background information on the sampling, resolution and accuracy of this unique type of observation.

Text S1. Airborne radio occultation geometry

The ARO geometry and schematic representation of the tangent point drift is described in Figure S1 below.

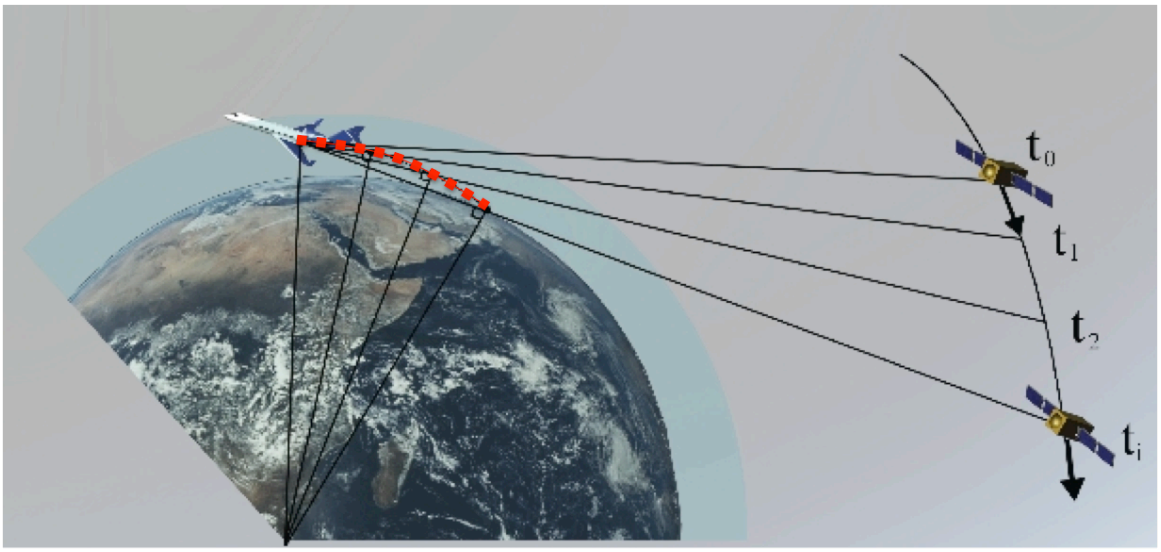

Figure S1. Airborne radio occultation geometry. GNSS signals are recorded as a satellite sets (or rises), with ray paths successively sampling deeper into the atmosphere. The points of closest approach of each ray path to the Earth's surface (tangent points) drift horizontally away from the aircraft as altitude decreases for a setting satellite (red dots). The atmosphere is most dense at the tangent point, so the measured refractive delays are most strongly influenced by the atmospheric properties at this location. Retrievals of atmospheric refractivity are represented as values along these slanted tangent point profiles (from Haase et al., 2014).

Text S2. Horizontal Resolution.

For a raypath with tangent point at 4 km the accumulated fraction of excess phase increases rapidly from zero to 50% within 1.4 km altitude of the tangent point, and the majority of the remaining excess phase is accumulated over the remaining 6.6 km altitude from 5.4 km to 12 km (Figure S2). As described in Kursinski et al., 1997, this is considered a useful approximate measure of vertical resolution and is close to the Fresnel resolution. The horizontal range spanned by the raypath in that interval is +/- 150 km of the raypath tangent point, and is approximately half the total distance the partial ray path travels in the atmosphere below flight level, which in this case is about +/- 340 km of the tangent point.

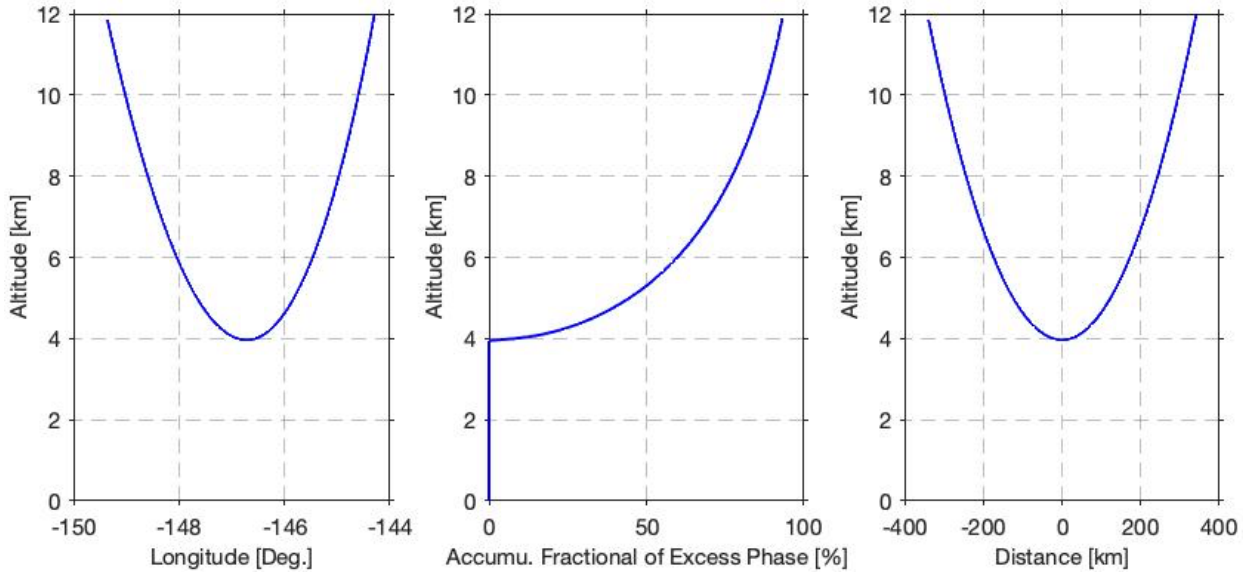

Figure S2. Excess phase accumulation for a ray with tangent point at 4 km assuming refractivity structure from dropsonde profile 2018-01-27-0030_38.7N_140.9W. From the center plot, 50% of the excess phase is accumulated from ~ 4 km to 5.4 km height. From the right plot, the ray travels +/- 150 km over the height range from 4 km to 5.4 km height.

We calculate the excess phase accumulation for all raypaths with tangent point elevation ranging from 0.5 to 11.5 km altitude. Then the values of dz and dL corresponding to 50% of the total accumulated excess phase are plotted in blue in Figure S3. (left) Shown in blue is the height interval (dz) over which 50 % of the excess phase is accumulated for the ray path with tangent height shown on the vertical axis, assuming the refractivity structure from a typical dropsonde profile, such as 2018-01-27-0030_38.7N_140.9W. Red dashed line is the diameter of the first Fresnel zone (right) 50% of the excess phase is accumulated over the ray path within +/- the distance dL from the tangent point, calculated numerically and shown in the blue line. Black dashed line is the horizontal resolution calculated from eq 13 and the vertical resolution. Red dashed line is calculated from eq 13 and the Fresnel resolution..

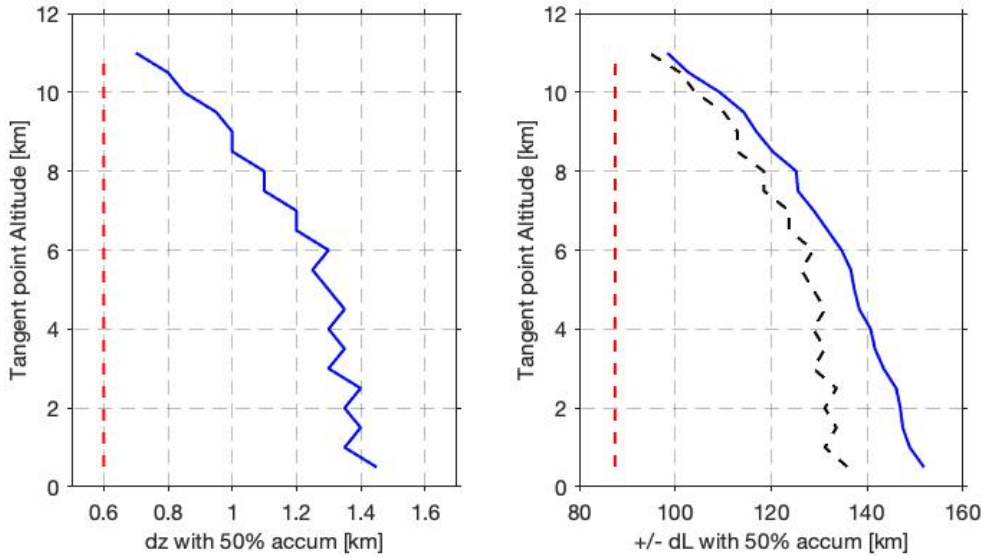

Figure S3. (left) Shown in blue is the height interval (dz) over which 50 % of the excess phase is accumulated for the ray path with tangent height shown on the vertical axis, assuming the refractivity structure from a typical dropsonde profile, such as 2018-01-27-0030_38.7N_140.9W. Red dashed line is the diameter of the first Fresnel zone (right) 50% of the excess phase is accumulated over the ray path within +/- the distance dL from the tangent point, calculated numerically and shown in the blue line. Black dashed line is the horizontal resolution calculated from eq 13 and the vertical resolution. Red dashed line is calculated from eq 13 and the Fresnel resolution.

Kursinski et al. (1997) provides an approximate expression for the relation between the horizontal and vertical resolution

$$\Delta L = 2(2R\Delta z)^{1/2} \quad \text{(eq 13 from Kursinski et al., 1997)}$$

where ΔL is horizontal resolution, Δz is the vertical resolution, and R is the radius to the tangent point altitude. This estimate of horizontal resolution is shown in the black dashed line in Figure S3, calculated from the estimate of dz in the left panel.

Kursinski et al. (1997) also provides the definition of the diameter of the first Fresnel zone, ZF , as a better estimate of the vertical resolution, neglecting the defocusing factor:

$$Z_F = 2[\lambda L_T L_R/(L_T + L_R)]^{1/2} \quad \text{(eq 14 from Kursinski et al., 1997)}$$

For a receiver at 14 km altitude above the surface $L_R \cong 420$ km and $L_T \cong 28500$ km, this gives a value of ~600 m for the theoretical vertical resolution (red dashed line in Figure S3) The corresponding horizontal resolution based on equation 13 from Kursinski et al., 1997 is estimated to be +/- 90 km of the tangent point location.

Text S3. Relationship between refractivity and temperature and humidity errors.

We describe the relation between error in refractivity (N%) and error in temperature (dT) and humidity (dq) with the analysis below. First we present the range of temperature and moisture profiles sampled with six IOPs from AR Recon 2018. The range of temperature at any height is greater than 20 K. The range of q between 2 and 8 km height is a factor of 100. Below 1 km the range of q is a factor of 5. Above 8 km, aside from the points with extremely low specific humidity, profiles group together closely and have a range of q on the order of a factor of 5 or less. We select two profiles for further analysis.

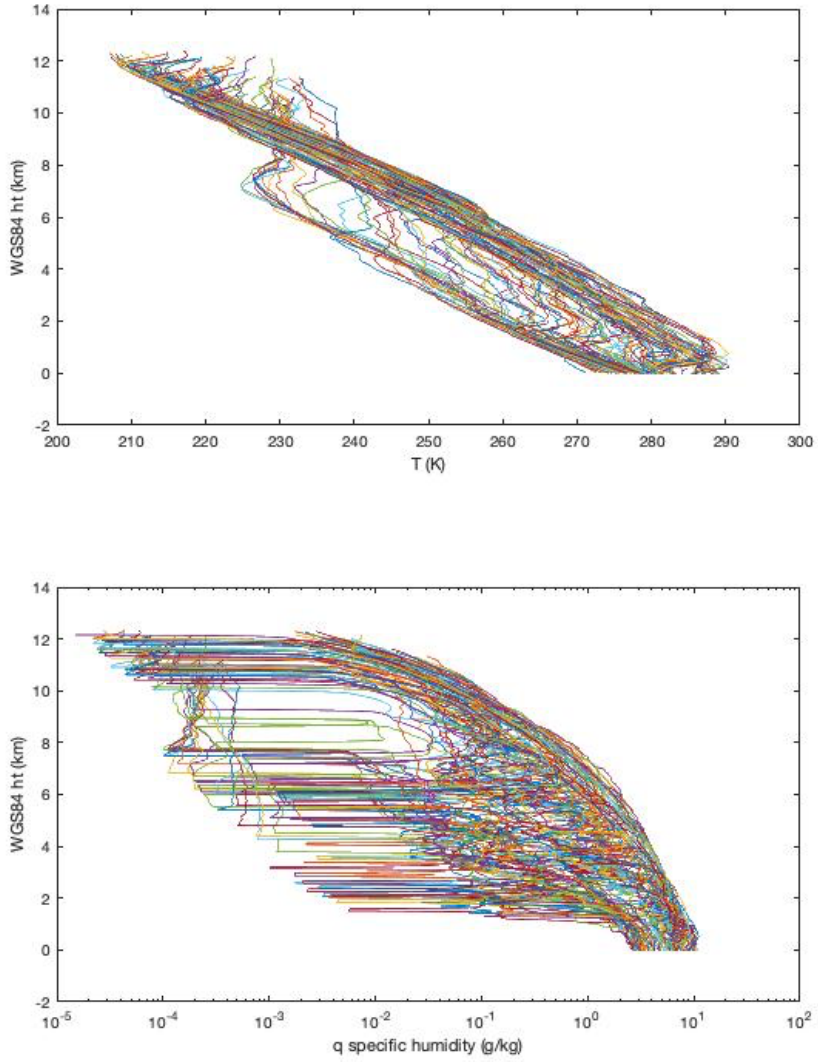

Figure S4. (top) all NOAA G-IV dropsonde temperature profiles from the six IOPs during AR Recon 2018. (bottom) all NOAA G-IV dropsonde specific humidity profiles from AR Recon 2018. Values of q below 10-2 are due to artifacts in the raw observations and were not included in the dropsonde analysis.

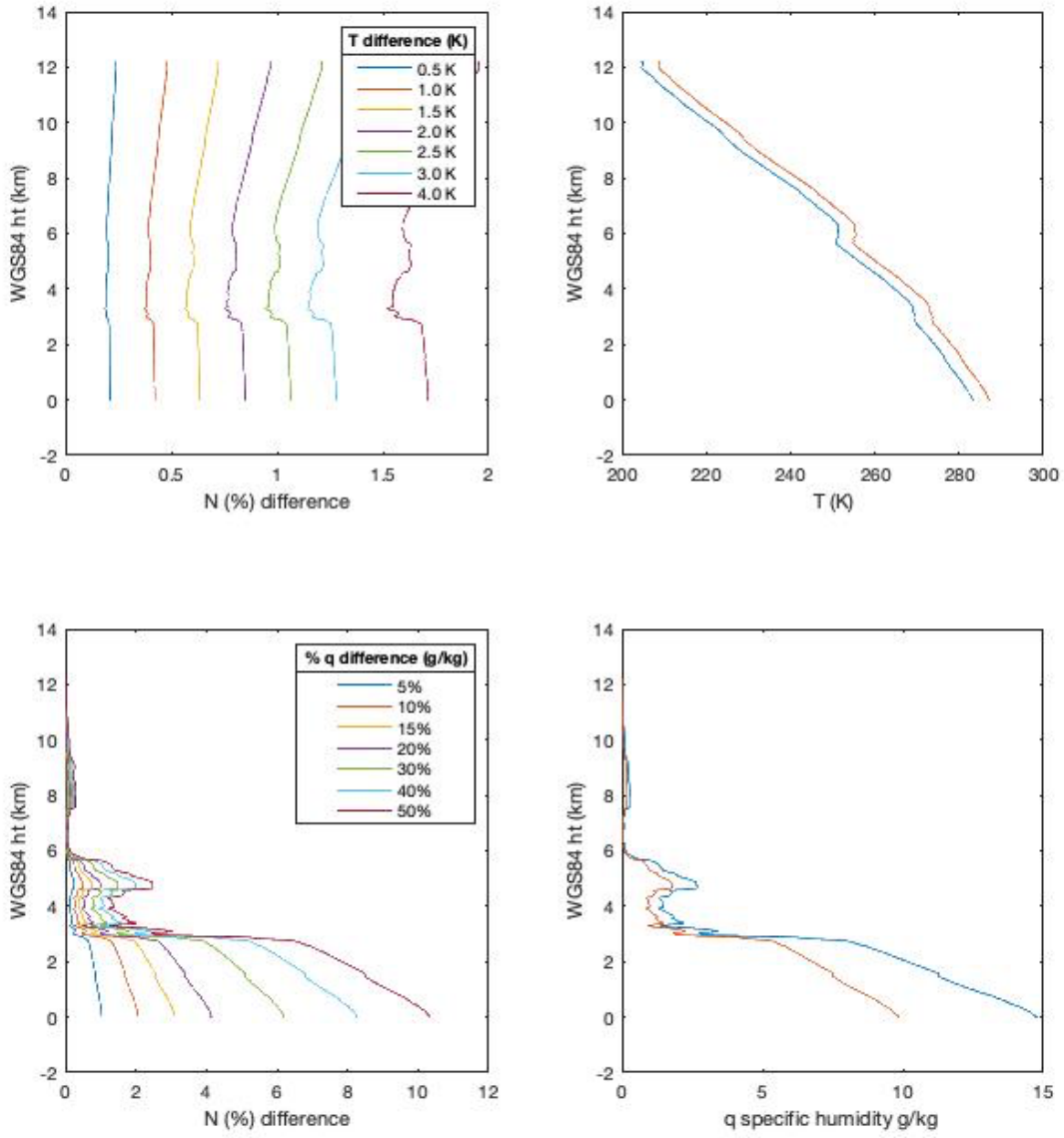

Figure S5. Relation between error in refractivity (N%) and error in temperature (dT) and humidity (dq) calculated from a typical dropsonde profile sampling the center of the AR. (top left) A refractivity difference of 0.6% N (the precision of two observations from different receivers) corresponds approximately to a temperature difference of 1.5 K. (top right) The dropsonde temperature profile and the temperature profile perturbed by 4 K. (lower left) For this profile, 0.6% N corresponds to less than 5% difference in specific humidity below 3 km and about 20% difference in specific humidity from 3-6 km. (lower right) The dropsonde q profile and the q profile perturbed by 50%. The precision of 0.6%N is much lower than the variability seen in the distribution of profiles in
Figure S4. .

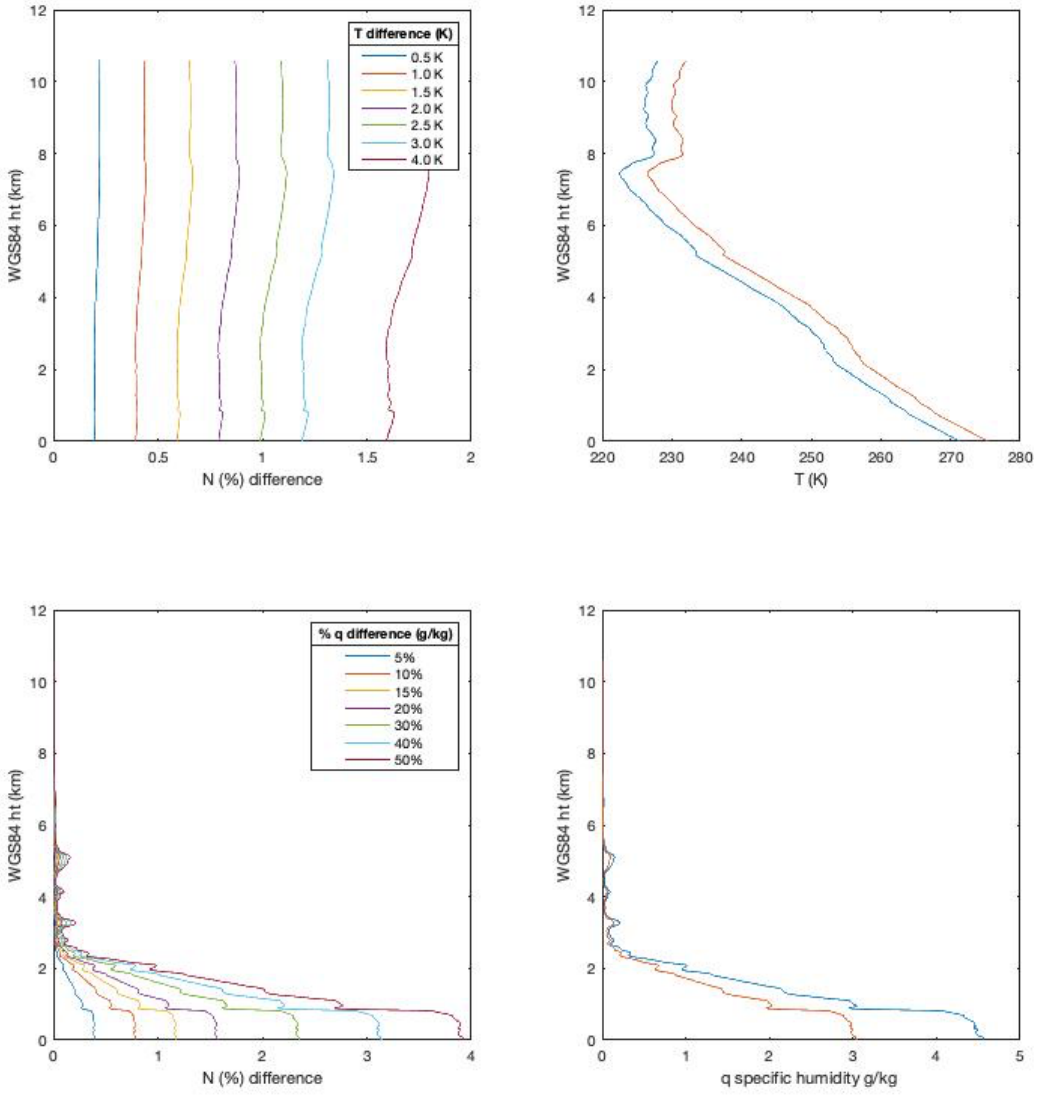

Figure S6. Similar relation between error in refractivity (N%) and error in temperature (dT) and humidity (dq) calculated from a typical dropsonde profile sampling the northern edge of the AR. (top left) A refractivity difference of 0.6% N corresponds approximately to a temperature difference of 1.5 K. (top right) The dropsonde temperature profile and the temperature profile perturbed by 4 K. (lower left) For this profile, 0.6% N corresponds to about 10% difference in specific humidity at the surface, then increasing to about 50 % at 2 km. (lower right) The dropsonde q profile and the q profile perturbed by 50%. The 0.6%N precision does not allow distinguishing variations in humidity at levels less than 0.5 g/kg. Variations of q in the height range 2 to 7 km are as much as a factor of 100 which are much greater than the 0.6% precision.

In summary, above 8 km even though there is a factor of 5 variability in the specific humidity all of the contributions of the moisture to the refractivity are below the error level of the refractivity measurement so ARO would contribute no information on moisture above that level. From about 3 to 8 km the contributions of specific humidity to refractivity are on the same order as the refractivity error. 0.6 % N error corresponds to about 10-20% error in q. However the variations in specific humidity are so large (a factor of 100) that they are easily detectable. Below 3 km the 0.6% N error corresponds to 5% error in q and a more important limitation than the error is the tracking of the signal below the boundary layer, which requires open loop tracking.

Text S4. RO observation error estimate from dropsonde comparisons

Comparisons of RO datasets from COSMIC-2, Other LEO RO missions, and ARO with collocated dropsondes provide insight into how well RO represents the 1-D refractivity structure of the atmosphere at a point location. Dropsondes were within 300 km and 2 hours of the RO profiles, using the same criteria as Ho et al., 2021. When multiple soundings were available, the closest sounding was used. From this perspective, ARO errors are comparable to LEO RO within the troposphere. For the purpose of selecting an observation error to use in the data assimilation experiment, it is reasonable to choose the same refractivity observation error as is used for data assimilation of LEO RO observations when using a refractivity operator.

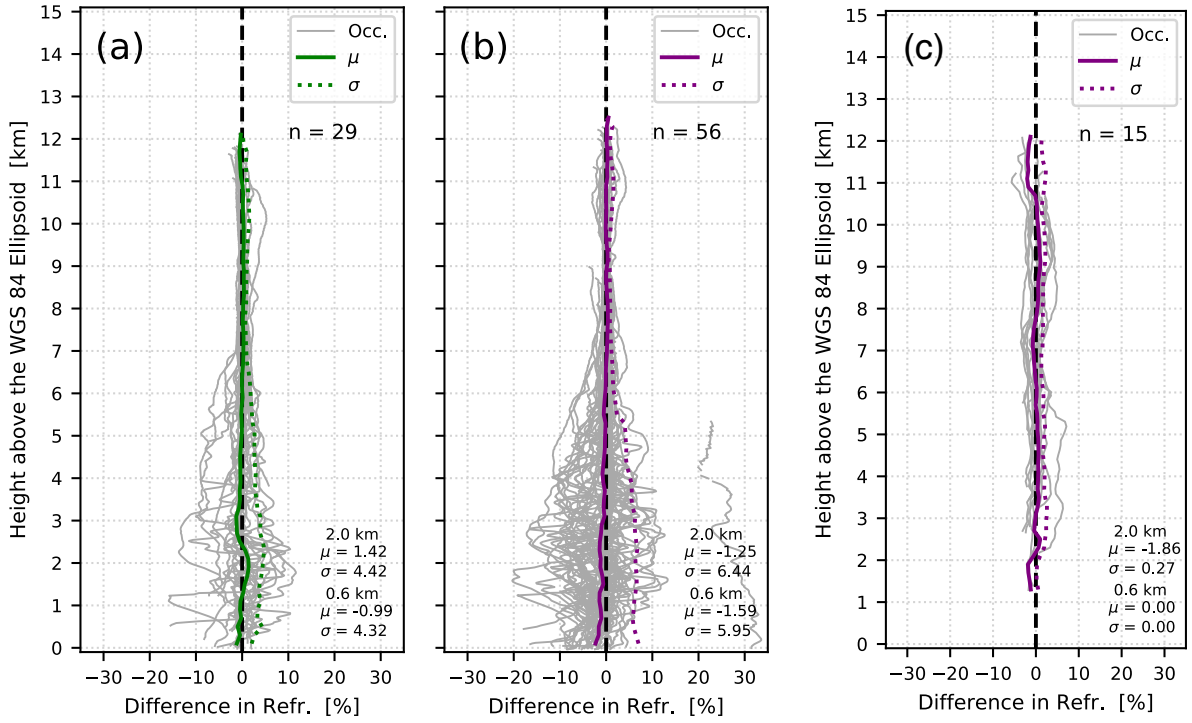

Figure S7. Statistical comparison between occultations and the nearest dropsonde that was within a distance threshold of 300 km and a time threshold of 2 hours during AR Reconnaissance. The percent difference in refractivity (%N) is shown between each occultation from (a) operational RO constellations without COSMIC-2, (b) COSMIC-2, and (c) ARO collected during AR Recon 2018 IOP01 and its corresponding dropsonde profile (grey lines), along with the mean and standard deviation of these differences (solid and dashed colored lines, respectively) computed in vertical bins with width of 200 m. The thick dashed black line highlights the line of zero difference and the number of sample pairs, n, for each dataset is indicated.

ARO - dropsondes (2018 IOP01)					**COSMIC-2 - dropsondes (2019-2020 all IOPs)**					**Other LEO RO - dropsondes (2019-2020 all IOPs)**			
ht (km)	N difference (%)		# obs		ht (km)	N difference (%)		# obs		ht (km)	N difference (%)		# obs
	mean	std dev				mean	std dev				mean	std dev	
1.0	-	-	-		1.0	-1.3	6.0	69		1	-0.4	3.7	18
2.0	-1.2	0.6	2		2.0	-1.2	6.4	78		2	1.4	4.5	24
3.0	-0.1	2.5	7		3.0	-0.7	6.2	79		3	-1.2	3.9	24
4.0	0.5	2.0	11		4.0	-0.7	5.2	81		4	-0.4	2.9	26
5.0	0.4	2.0	13		5.0	-0.2	4.2	82		5	-0.1	2.7	27
6.0	0.2	1.7	15		6.0	-0.2	1.7	81		6	0.0	1.8	29
7.0	-0.6	1.4	15		7.0	0.2	1.1	80		7	0.3	0.9	29
8.0	0.3	1.6	15		8.0	0.4	0.9	73		8	0.2	0.8	23
9.0	1.0	2.0	15		9.0	0.2	0.7	33		9	0.3	1.0	15
10.0	0.5	1.8	15		10.0	-0.1	1.0	30		10	0.3	1.5	14
11.0	-1.9	2.1	5		11.0	0.1	1.6	29		11	-0.1	1.1	13
12.0	-1.4	1.3	3		12.0	0.1	0.9	9		12	-0.4	0.2	1
Overall	-0.1	1.8			Overall	-0.1	2.4			Overall	-0.1	1.7	
(above 2 km)					(above 2 km)					(above 2 km)			

Table S1. Statistical comparison between occultations and the nearest dropsonde as a function of height.

Text S5. Analysis increment

The ARO data have the effect of spreading the increment into the space between the different flight tracks as shown in this enlarged view.

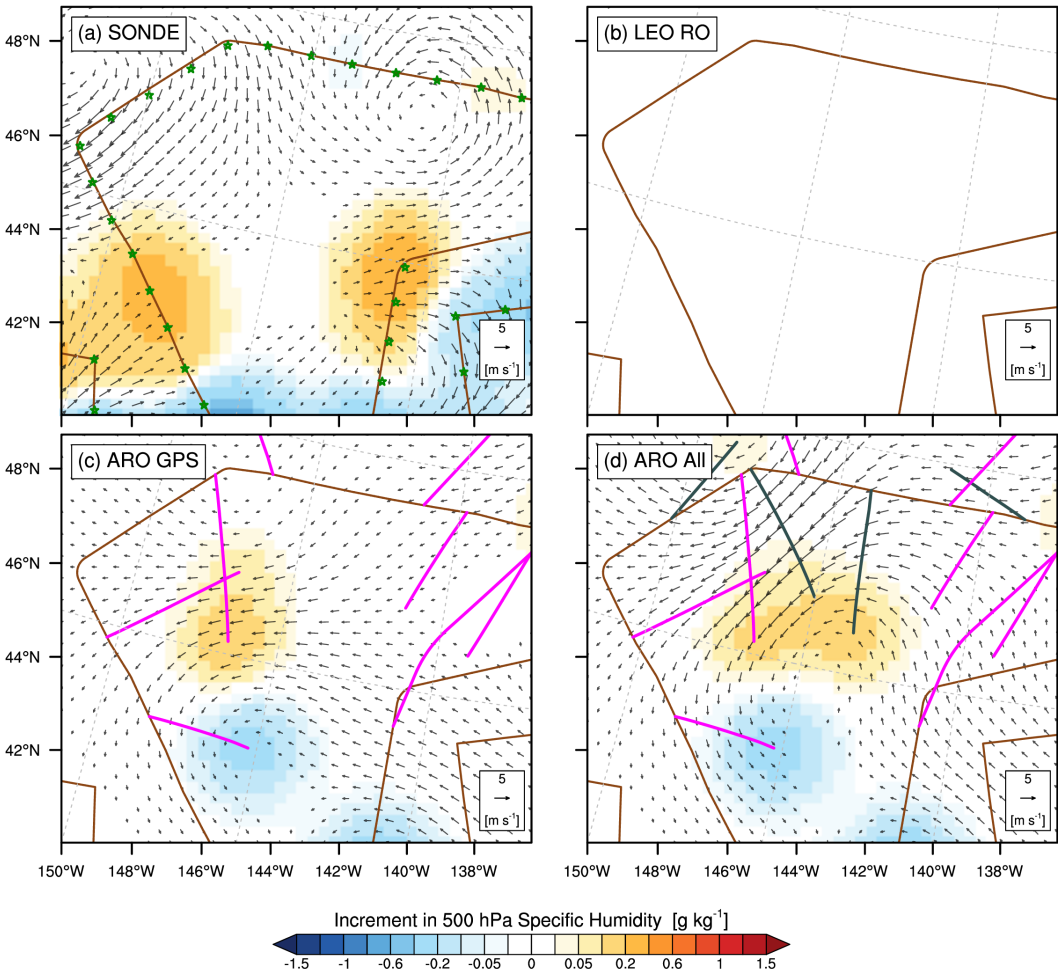

Figure S8. Enlarged view of the WRF analysis increment in moisture on the 500 hPa surface at 00 UTC 27 Jan 2018 a) after assimilation of dropsondes and radiosondes and b) LEO RO, c) ARO observations from GPS only, and d) ARO observations from GPS + Galileo illustrating the increment produced off the flight track.

Text S6. Impact on Precipitation Forecast

The GFS model assimilates data from many satellite, ocean, land, and in-situ observing systems and has been finely tuned to optimize performance over North America. For the context of this work, it is not feasible to replicate the entire observing system to carry out data denial experiments and evaluate precipitation impact with a statistically rigorous method for a single event. The data assimilation increment is complementary to that of dropsondes, which have been shown to improve forecasts (Stone et al., 2020). This supports the argument that the ARO observations, which can be collected whenever dropsonde reconnaissance flights are deployed, merit comprehensive data impact experiments. We show the impact on 6 hour accumulated precipitation for 06Z to 12Z on 27 January. The difference in forecast specific humidity is largest off the coast of California which reinforces the drier tendency in a region where precipitation is not heavy. On the other hand, the forecast precipitation is increased in southern Oregon at the time the AR makes landfall when the ARO observations are assimilated, versus the dropsondes, so there is some additional information that is being contributed to the forecast.

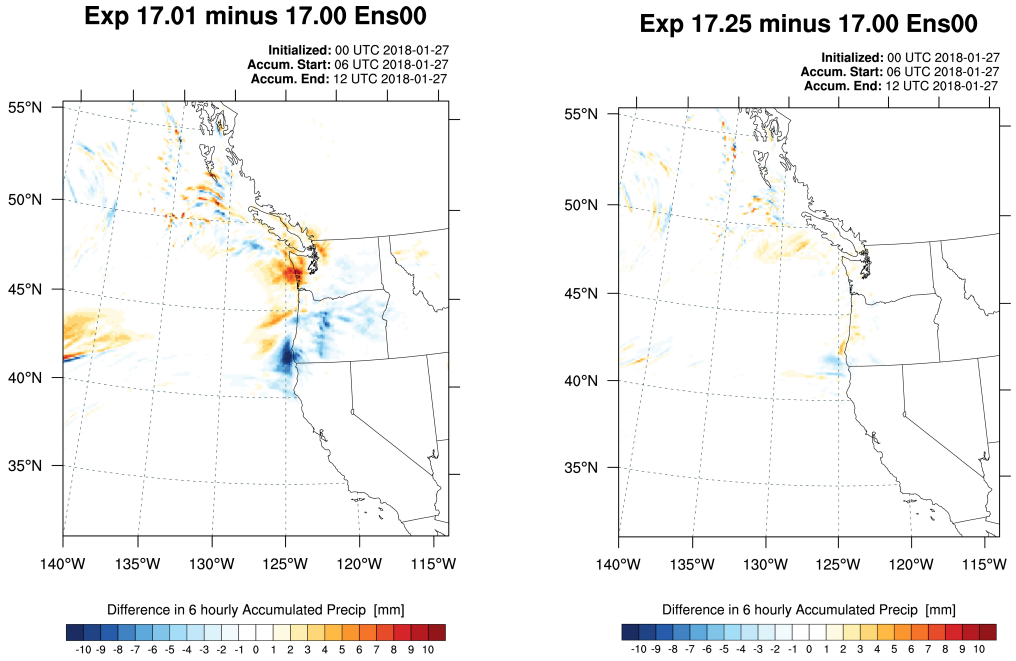

Figure S9. Difference in 6 hour accumulated precipitation for 06Z to 12Z on 27 January for dropsonde minus the no-DA experiment (left) and the ARO minus no-DA experiment (right).

Text S7. Model comparison statistics for AR Recon 2018 RF01

In this case, the bias seen in the ECMWF model (a) above 5 km was reduced in the high resolution dropsonde experiment (b) relative to the independent ARO observations. Because the ARO observations are concentrated in a limited area, it is not likely that this represents a global bias in the ECWMF model. It is more likely that the dropsondes improved the model near the areas that the ARO observations were measuring for this specific case, and more case studies should be carried out.

a)

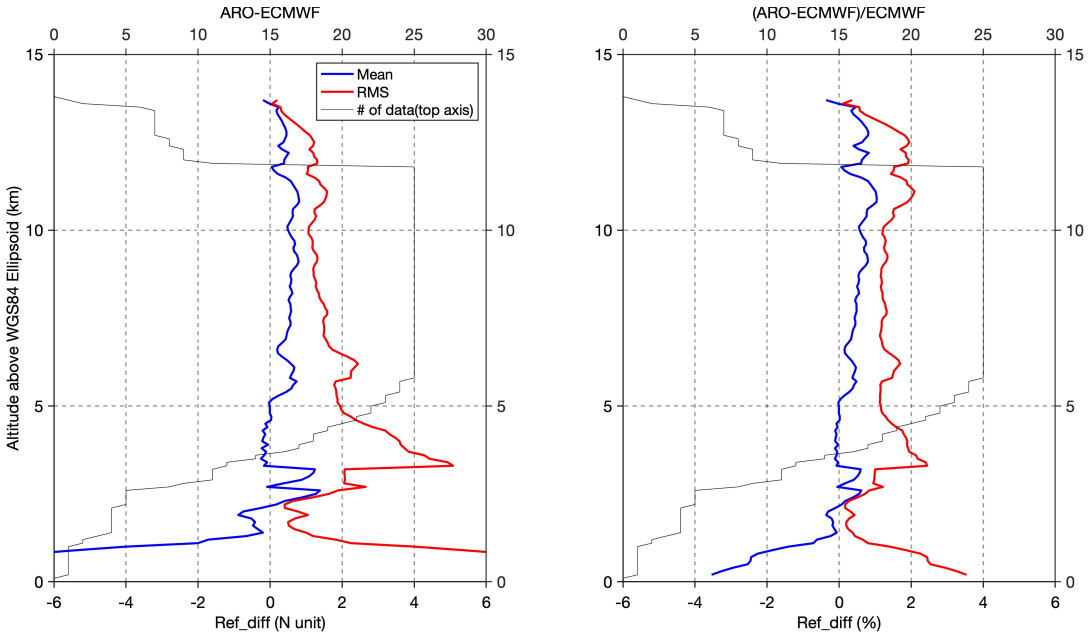

b)

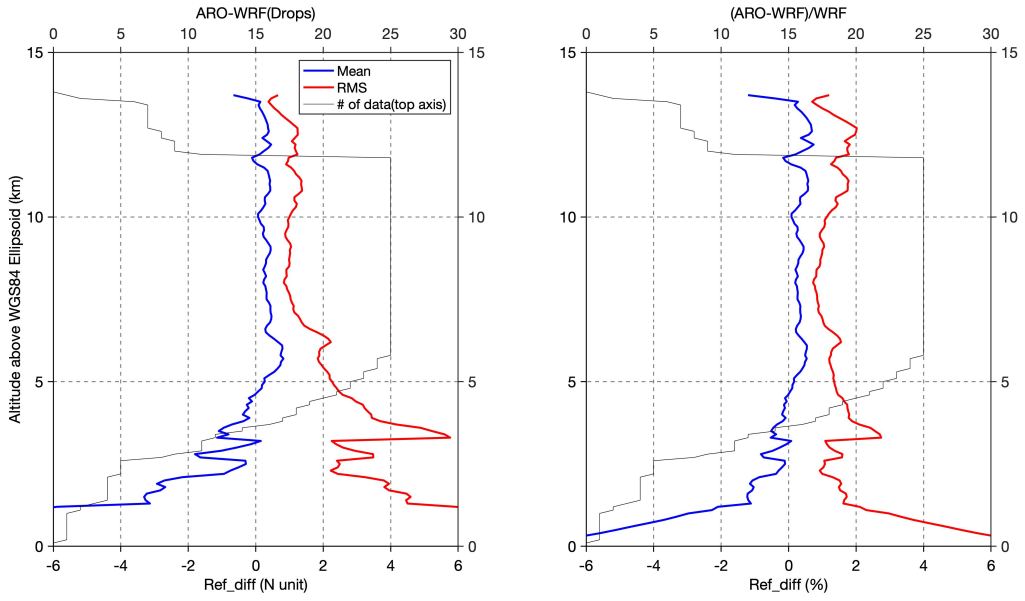

c)

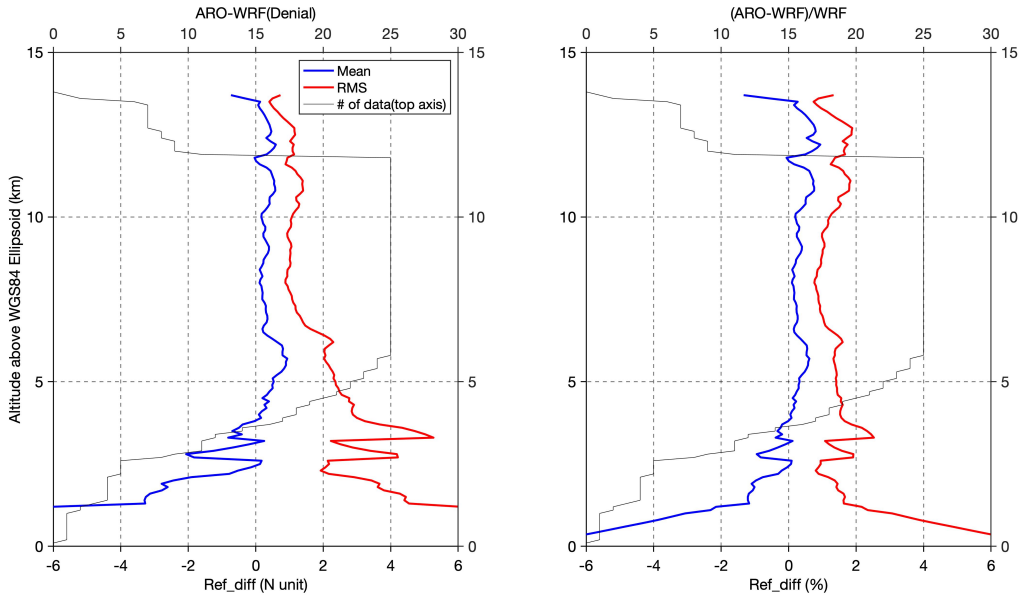

Figure S10. Statistical comparison between model output and ARO observations a) ARO minus ERA5 mean and standard deviation b) ARO minus WRF Dropsonde assimilation experiment, c) ARO minus WRF No DA experiment, all valid at 00 UTC 27 January 2018.

Text S8. Dropsonde DA experiment

The dropsonde data extend to the surface and measure directly temperature and moisture. As a result the moisture increments are larger than the ARO increments, especially below 4 km. The negative refractivity increment in the DROPS-NoDA case, for example, at ~40N and about 5 km height, extends to the south at much lower altitudes than in the ARO-NoDA case (Figure 8b) where the ARO observations do not reach. There are also differences due to the fact that the dropsondes are not sampling the same transect as the ARO observations.

a)

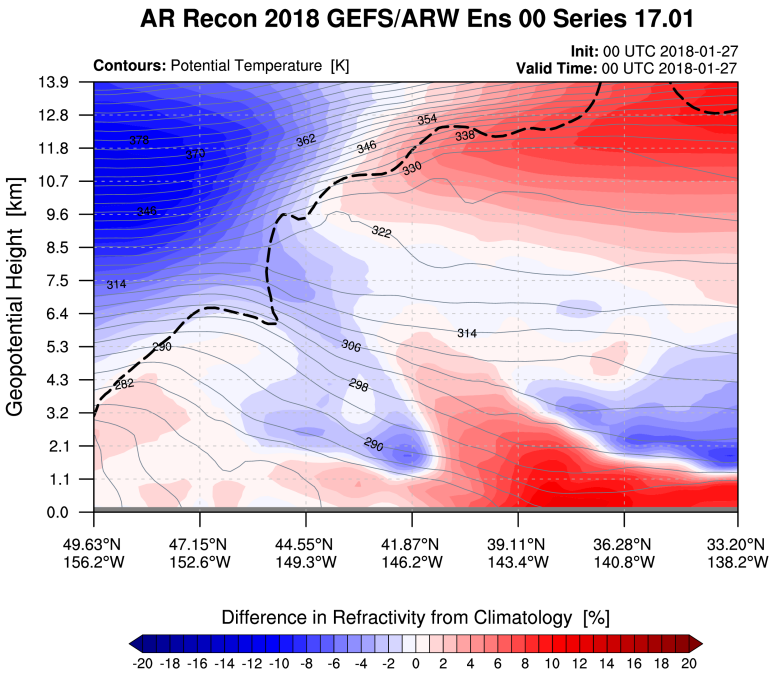

b)

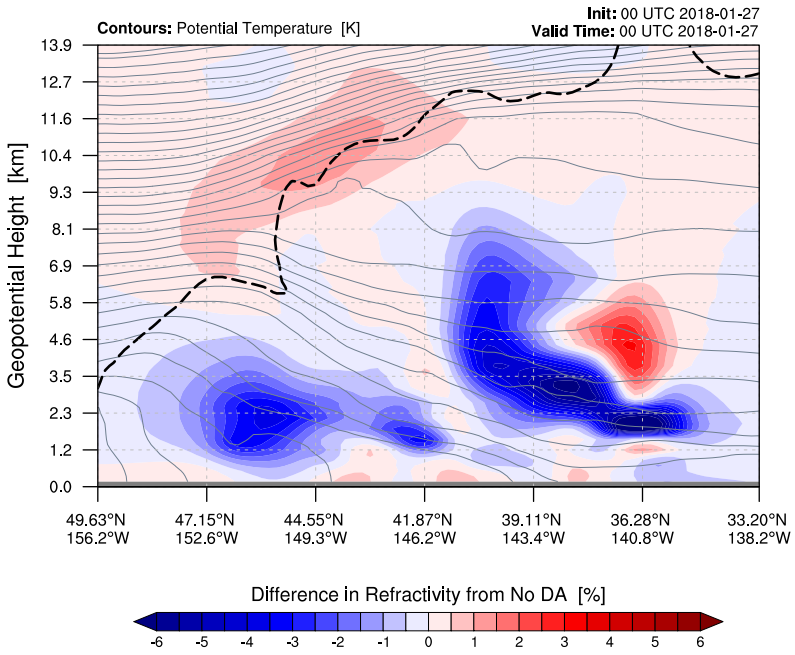

Figure S11. a) Refractivity anomaly cross-section through the WRF model DROPS experiment, beneath the western dropsonde transect across the AR; Refractivity anomaly (%) is the difference from a climatological model. The actual 2 PVU contour is represented by the thick black dashed line. Potential temperature contours are shown in gray. b) difference in refractivity between the DROPS and NoDA experiments.

Text S9. ARO Flight animation

The geometry of rising and setting occultations are illustrated in Figure S12, and an animation of the IOP01 flight accompanies the manuscript, ar18_rf01_aro_drop.mp4.

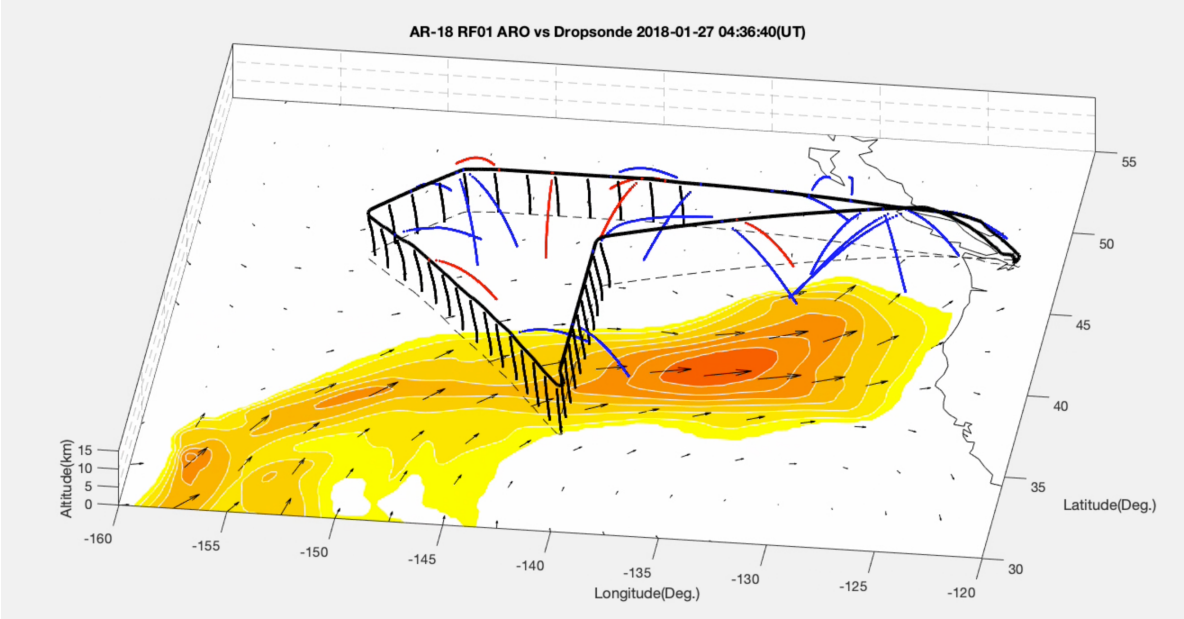

Figure S12. As the aircraft flies along the trajectory (brown line), dropsondes are released below the aircraft shown by the black vertical lines. Each curved blue line shows the location of the tangent points for a GPS or Galileo satellite occultation. The highest tangent point is near the aircraft flight path, and the tangent points drift further from the flight track as they descend. There is one blue curve for each setting satellite occultation and one red curve for each rising satellite occultation. IVT is illustrated in color contours on the lower surface.

Movie S1 Caption. As the aircraft flies along the trajectory (brown line), dropsondes are released below the aircraft shown by the black vertical lines. Each curved blue line shows the location of the tangent points for a GPS or Galileo satellite occultation. The highest tangent point is near the aircraft flight path, and the tangent points drift further from the flight track as they descend. There is one blue curve for each setting satellite occultation and one red curve for each rising satellite occultation. IVT is illustrated in color contours on the lower surface.